



# Effects of Long Term Exposures on PM Disk Superalloys

*T.P. Gabb, C.K. Sudbrack, S.L. Draper, R.A. MacKay, and J. Telesman  
Glenn Research Center, Cleveland, Ohio*

## NASA STI Program . . . in Profile

Since its founding, NASA has been dedicated to the advancement of aeronautics and space science. The NASA Scientific and Technical Information (STI) program plays a key part in helping NASA maintain this important role.

The NASA STI Program operates under the auspices of the Agency Chief Information Officer. It collects, organizes, provides for archiving, and disseminates NASA's STI. The NASA STI program provides access to the NASA Aeronautics and Space Database and its public interface, the NASA Technical Reports Server, thus providing one of the largest collections of aeronautical and space science STI in the world. Results are published in both non-NASA channels and by NASA in the NASA STI Report Series, which includes the following report types:

- **TECHNICAL PUBLICATION.** Reports of completed research or a major significant phase of research that present the results of NASA programs and include extensive data or theoretical analysis. Includes compilations of significant scientific and technical data and information deemed to be of continuing reference value. NASA counterpart of peer-reviewed formal professional papers but has less stringent limitations on manuscript length and extent of graphic presentations.
- **TECHNICAL MEMORANDUM.** Scientific and technical findings that are preliminary or of specialized interest, e.g., quick release reports, working papers, and bibliographies that contain minimal annotation. Does not contain extensive analysis.
- **CONTRACTOR REPORT.** Scientific and technical findings by NASA-sponsored contractors and grantees.

- **CONFERENCE PUBLICATION.** Collected papers from scientific and technical conferences, symposia, seminars, or other meetings sponsored or cosponsored by NASA.
- **SPECIAL PUBLICATION.** Scientific, technical, or historical information from NASA programs, projects, and missions, often concerned with subjects having substantial public interest.
- **TECHNICAL TRANSLATION.** English-language translations of foreign scientific and technical material pertinent to NASA's mission.

Specialized services also include creating custom thesauri, building customized databases, organizing and publishing research results.

For more information about the NASA STI program, see the following:

- Access the NASA STI program home page at <http://www.sti.nasa.gov>
- E-mail your question to [help@sti.nasa.gov](mailto:help@sti.nasa.gov)
- Fax your question to the NASA STI Information Desk at 443-757-5803
- Phone the NASA STI Information Desk at 443-757-5802
- Write to:  
STI Information Desk  
NASA Center for AeroSpace Information  
7115 Standard Drive  
Hanover, MD 21076-1320



# Effects of Long Term Exposures on PM Disk Superalloys

*T.P. Gabb, C.K. Sudbrack, S.L. Draper, R.A. MacKay, and J. Telesman  
Glenn Research Center, Cleveland, Ohio*

National Aeronautics and  
Space Administration

Glenn Research Center  
Cleveland, Ohio 44135

## Acknowledgments

Richard Rogers and Laura Evans of NASA Glenn Research Center are acknowledged for determination of near-surface phases by x-ray diffraction and their composition by electron microprobe, respectively. Ronald Phillips of Vantage Partners, LLC is acknowledged for his aid in running tensile tests in vacuum at NASA Glenn Research Center. Timothy Gorman of University of Dayton and Devon Beckett of Drexel University are acknowledged for SEM evaluations of some coupons given static exposures and for measurements of layer thicknesses.

*Level of Review:* This material has been technically reviewed by technical management.

Available from

NASA Center for Aerospace Information  
7115 Standard Drive  
Hanover, MD 21076-1320

National Technical Information Service  
5301 Shawnee Road  
Alexandria, VA 22312

Available electronically at <http://www.sti.nasa.gov>

# Effects of Long Term Exposures on PM Disk Superalloys

T.P. Gabb, C.K. Sudbrack, S.L. Draper, R.A. MacKay, and J. Telesman  
National Aeronautics and Space Administration  
Glenn Research Center  
Cleveland, Ohio 44135

## Abstract

Turbine disks in some advanced engine applications may be exposed to temperatures above 700 °C for extended periods of time, approaching 1,000 h. These exposures could affect the near-surface composition and microstructure through formation of damaged and often embrittled layers. The creation of such damaged layers could significantly affect local mechanical properties. Powder metal disk superalloys LSHR and ME3 were exposed at temperatures of 704, 760, and 815 °C for times up to 2,020 h, and the types and depths of environmental attack were measured. Fatigue tests were performed for selected cases at 704 and 760 °C, to determine the impact of these exposures on fatigue life. Fatigue resistance was reduced up to 98% in both superalloys for some exposure conditions. Tensile tests were also performed to help understand fatigue responses, and showed corresponding reductions in ductility. The changes in surface composition and phases, depths of these changed layers, failure responses, and failure initiation modes were compared.

## Introduction

To screen the fatigue resistance of nickel-based disk superalloys, conventional low cycle fatigue tests are often performed with cycles having periods of 0.1 to 120 s, in the interests of combining cyclic lives of up to 10,000 cycles with affordable test durations of near 100 h. However, environmental exposures at high temperatures of 650 to 815 °C in actual service can approach 1000 h in aerospace gas turbine engines, and 10,000 h in land-based gas turbine engines. The disk temperatures in both classes of engines are anticipated to rise, as higher compressor discharge air temperature is known to improve fuel efficiency and performance (Ref. 1). Turbine disk rims are cooled by compressor discharge air, and their temperature tracks closely with compressor discharge air temperature.

Exposures at a temperature of 870 °C have been shown to produce significant reductions in fatigue resistance of blade superalloy Rene 80 (Ref. 2). Oxide layers were identified as the cause, along with an underlying region where  $\gamma'$  precipitates had been dissolved. Fatigue lives could be largely recovered by removing the oxidized layers. Exposures at disk application temperatures of 650 to 704 °C have also been shown to reduce fatigue lives of powder metal disk superalloys Udimet 720 and ME3 (Ref. 3). It was shown that the exposures could cause a change in the locations of failure initiation sites from internal flaws to surface oxidation damage, which in turn reduced the fatigue lives. However, this response was intermittent depending on exposure conditions, and often confounded the effects of exposures with that of crack location on fatigue life. It has often been observed that disk fatigue specimens failing from cracks initiating at defects on the surface have lower corresponding fatigue lives than those failing from internal cracks initiating at defects far from the surface (Ref. 4). This has been associated with differences in stress intensity due to longer surface crack initiation sites, and environmental interactions for accelerated crack initiation and growth at surface versus internal cracks (Ref. 5). More recent evaluations of exposure effects on disk superalloys have been performed on notched fatigue specimens, where the stress concentration of the notch encourages cracking at the notch root. Here, the superalloy RR1000 (Ref. 6) was shown to form recrystallized grains with porosity within the underlying region where  $\gamma'$  precipitates had been dissolved, while ME3 (Ref. 7) instead had fingers of  $\text{Al}_2\text{O}_3$  extending into a recrystallized zone. Both alloys had significant reductions in fatigue life after exposures at 700 to 815 °C. However, it is not clear if these exposure effects were enhanced by the concentrated stresses at the exposed notch surfaces.

The objective of this study was to screen the effects of high temperature exposures in air on the microstructure and fatigue properties of two powder metal disk superalloys. Fully machined mechanical test specimens of LSHR and ME3 were exposed at 704, 760, and 815 °C, for times up to 2,020 h. Uniform gage and notch gage fatigue tests were performed at 704 or 760 °C, allowing the effect of concentrated notch stresses to be ascertained. Tensile tests were subsequently performed to further investigate cracking of the identified environment-affected surface layers. The effects of exposures on fatigue life, tensile strength, and tensile elongation were compared. The associated failure modes and their relationships to exposure-induced changes in compositions and phases near the surface were determined.

## **Materials and Test Procedures**

### **Materials**

The compositions in weight percent of the tested materials are listed in Table 1. The compositions of LSHR and ME3 are similar, with the biggest differences in Mo, Nb, Ta, and W contents. LSHR contains less Mo and Ta, but more W and Nb than ME3. LSHR (Ref. 8) superalloy powder was obtained from Special Metals Corp. This powder was atomized in argon, screened to -270 mesh, sealed in a stainless steel container, and then consolidated by hot isostatic pressing. The consolidated material was subsequently extruded and isothermally forged into several flat disks. Stacked rows of rectangular blanks each about 13 mm square and 66 mm long were extracted throughout the forged disks, with their lengths oriented parallel to the disk plane. The blanks were placed vertically within an enclosing fixture and supersolvus solution heat treated at 1171 °C for 2 h in a resistance heating furnace. The assembly of blanks and enclosing fixture was then removed to cool in static air. This gave a near-linear cooling rate of the blank cores, averaging 72 °C per minute cooling rate down to 870 °C. The blanks were subsequently given an aging heat treatment of 855 °C for 4 h followed by 775 °C for 8 h. Blanks of similar dimensions were also extracted from the web and rim of several fully heat treated disks of ME3 (Ref. 7), which had been subjected to similar thermo-mechanical processing conditions. The ME3 blanks were selected from the disks at locations having comparable cooling rates after the solution heat treatment to that of the LSHR blanks. But unlike LSHR disks, the ME3 disks were fully heat treated before blank extraction, so ME3 blanks were directly machined into notch fatigue and tensile specimens.

Fatigue and tensile specimens were machined using low stress grinding procedures, with the gage sections finally polished parallel to the loading direction, in order to not exceed 0.21 µm average roughness. LSHR uniform gage fatigue specimens had a gage diameter of 4.8 mm across a gage length of 13 mm. ME3 cylindrical notched specimens (Fig. 1) had minimum diameter of 5.1 mm, with a geometric elastic stress concentration factor  $K_t = 2$ . Several LSHR specimens were also prepared with the cylindrical notch configuration of Figure 1, for consistent fatigue test comparisons with ME3. Accompanying LSHR and ME3 tensile specimens having a nominal gage diameter of 4.1 mm across a gage length of 21 mm were also machined.

### **Test Procedures**

Most exposures were conducted in conventional resistance heating box furnaces in lab air, with all specimens and blanks air cooled after exposures. Fully machined specimens were exposed after being wiped with cotton soaked in acetone, and then ethanol. Several additional exposure conditions were investigated, including: 1) oversized specimen blanks were sometimes exposed in air for selected long exposures at 704, 760, and 815 °C before machining into specimens, in order to assess the effects of the exposures on superalloy microstructure and properties remote from the surface; 2) fully machined ME3 notched gage fatigue specimens were wrapped with Ta foil to getter remnant oxygen and then were exposed in a vacuum pressure not exceeding  $9 \times 10^{-7}$  torr; 3) cyclic exposures in air were conducted on uniform-gage LSHR fatigue specimens to assess cyclic effects. All cyclic specimens were heated to 815 °C and cooled to approximately 32 °C. Here, the machined specimens were suspended from a

horizontal alumina tube while a standard resistance-heating horizontal tube furnace automatically translated over the specimens during the 60 min heating cycle. The furnace automatically translated away from the specimens during the 20 min cooling cycle, to cool in static air. A typical heating and cooling cycle is shown in Figure 2, showing outputs from attached platinum–rhodium “Type R” thermocouples. These specimens were exposed to 440 cycles.

LSHR and ME3 were tested in different, yet complementary manners to screen the effects of the exposures on fatigue life for two different fatigue conditions. Fatigue tests of LSHR specimens with uniform gages were performed at 760 °C, and tests of ME3 specimens with notched gages were performed at 704 °C. Temperature was measured using chromel–alumel “Type K” thermocouples contacting the specimens. Fatigue tests were performed in accordance with fatigue test specification ASTM E466-07. All fatigue tests used a sinusoidal waveform cycling stress at a constant frequency of 0.33 Hz. LSHR specimens were tested using a uniaxial electro-mechanical testing machine having a resistance heating furnace. A maximum stress of 841 MPa and minimum stress of –428 MPa was applied in all tests. Preliminary testing of LSHR showed these cyclic stresses are typical stabilized values generated in strain-controlled tests at a total strain range of 0.76 percent and minimum/maximum strain ratio of 0, which typically resulted in surface-initiated fatigue failures and limited the fatigue life for specimens without long prior exposures in air (Ref. 8). However, no extensometer for strain measurements was attached to the specimens in the present fatigue tests, in order to avoid contacting the exposed surfaces.

Fatigue tests of notched gage ME3 specimens were performed using uniaxial servo-hydraulic testing machines with resistance heating furnaces. A maximum stress of 855 MPa and minimum stress of 43 MPa were applied in all tests, which were performed at 704 °C. Previous testing of ME3 using this notched gage specimen with these test conditions produced mean fatigue lives of 24,000–78,000 cycles and encouraged transgranular surface-initiated fatigue cracks to limit fatigue. (Ref. 9). For all fatigue tests, one-way statistical analyses of variance in fatigue lives were performed using JMP Version 10 (SAS Institute Inc., Cary, NC, 1989–2013) software, to test for significant differences in mean life response. Stepwise multiple linear regressions were also performed using this software, with a 90% probability of significance required for inclusion of any variable. This software was used to “code” all variables (V), by normalizing them using Equation (1):

$$V = (V - V_{\text{mid}})/(V_{\text{range}}/2) \quad (1)$$

This normalized each variable  $V$  to values of –1 to 1, so comparisons could be made of the relative influence of each significant variable, by directly comparing the magnitudes of their coefficients in the regression equation (Ref. 10).

Tensile tests were performed in general accordance with ASTM E21-05 and ASTM G129-00. Tests on LSHR were performed at 704 and 760 °C in air on a servo-hydraulic testing machine, using a conventional resistance heating furnace. Tensile tests of LSHR performed at 760 °C used a displacement rate of 0.1041 mm/s, which produced an average strain rate  $5.0 \times 10^{-3} \text{ s}^{-1}$ , to simulate conditions experienced in the uniform gage fatigue tests. Companion tensile tests of LSHR were also performed at 704 °C with a much slower displacement rate of 0.0017 mm/s and average strain rate of  $8.3 \times 10^{-5} \text{ s}^{-1}$  per ASTM G129-00, to screen strain rate dependence and temperature dependence of exposure effects on tensile response. Tests on ME3 were performed at 704 °C in a vacuum chamber held at a vacuum pressure not exceeding  $8 \times 10^{-6}$  torr, integrated in an electro-mechanical universal testing machine. Resistance-heating elements were used to heat the specimen. These tensile tests in vacuum were performed at displacement rates of 0.0017 mm/s and 0.017 mm/s, which produced average strain rates of  $8.3 \times 10^{-5} \text{ s}^{-1}$  and  $8.3 \times 10^{-4} \text{ s}^{-1}$ , respectively. However, no extensometer for strain measurements was attached to the specimens in the tensile tests, to avoid contacting the exposed surfaces.

ASTM grain sizes were determined from etched metallographic sections using linear intercepts of circular grid overlaps on optical images in accordance with ASTM E112-10 linear intercept procedures using circular grid overlays on optical images. Precipitate microstructures were characterized using field

emission scanning electron microscopy on metallographically prepared and etched sections. Metallographic sections were swab etched with 25% acetic acid, 25% nitric acid, 25% HCl, 25% H<sub>2</sub>O, 1% HF by volume. While it is recognized that imaging of the finest tertiary  $\gamma'$  precipitates is compromised using this approach, it was still considered sufficient for this study to make relative comparisons among exposure conditions. The area of each precipitate was measured using SigmaScan Pro (Systat Software Inc., San Jose, CA) image analysis software by thresholding based on image brightness. The equivalent radius of a circular precipitate was also calculated from each precipitate's area. Fracture surfaces were examined to determine failure initiation sites using scanning electron microscopy.

## Results and Discussion

### Microstructures

#### Internal Microstructures

Internal microstructures for unexposed test materials are shown in Figure 3, including magnified views of the secondary and tertiary  $\gamma'$ -precipitates. Mean linear intercept ASTM grain size and the measured dimensions of the secondary and tertiary  $\gamma'$  precipitate are listed in Table 2. LSHR had a finer average grain size of 15  $\mu\text{m}$ , compared to ME3 at 29  $\mu\text{m}$ . Secondary  $\gamma'$  precipitates in LSHR were a mixture of rounded cubes and moderately extended cubes, having lobes growing at the corners. The area of each precipitate was measured, and the equivalent radius of a spherical particle is also compared in Table 2. ME3 predominantly had larger precipitates on either size basis, with much more extended growth of lobes at the cube corners. This was due to the different and slower initial cooling path after solution heat treatment for the ME3 disk material, heat treated as large disks (Ref. 11). Tertiary  $\gamma'$  precipitates were consistently near spherical, and slightly larger for ME3 than for LSHR. MC carbides were often observed along with fewer M<sub>3</sub>B<sub>2</sub> borides within grains of both superalloys, while MC and M<sub>23</sub>C<sub>6</sub> carbides and M<sub>3</sub>B<sub>2</sub> borides were observed along the grain boundaries of LSHR (Ref. 8 to 12).

Internal microstructures are also shown after an exposure of 815 °C at 2,020 h in Figure 3e and 3f. Secondary and tertiary  $\gamma'$  precipitate dimensions are also listed for this material condition in Table 2. Secondary  $\gamma'$  precipitate size increased after aging LSHR, while precipitate size actually decreased for ME3. This was apparently related to the stability of the highly extended, lobed precipitates in ME3. Work on other disk superalloys has shown these particle shapes can be unstable in certain exposure conditions, and that they evolved into smaller, more equiaxed shapes (Ref. 13). Tertiary  $\gamma'$  precipitates were no longer observed in both alloys, and were apparently dissolved during coarsening of secondary  $\gamma'$  precipitates. This was observed both for specimens and blanks subjected to this exposure.

#### Surface Microstructures

To assess influence of aging exposures on mechanical properties, surface microstructure were examined in detail. With increasing exposure time and temperature, oxides grew on the surfaces of LSHR and ME3 in a very similar manner, Figure 4 and Figure 5. Cross section evaluations of accompanying exposed coupons indicated that complex changes occurred near the surface during exposures for both ME3 and LSHR. Continuous Cr<sub>2</sub>O<sub>3</sub> was observed on the surface, along with faceted grains of TiO<sub>2</sub>. The TiO<sub>2</sub> grains became noticeably larger and more abundant with exposure time. Internal branched Al<sub>2</sub>O<sub>3</sub> fingers were evident beneath the outer Cr<sub>2</sub>O<sub>3</sub>-TiO<sub>2</sub> scale, even for the shortest exposures. These Al<sub>2</sub>O<sub>3</sub> fingers extended into a zone of the alloy that was recrystallized, and where  $\gamma'$  precipitates were also dissolved. The depth of  $\gamma'$  precipitate dissolution extended slightly further than the Al<sub>2</sub>O<sub>3</sub> fingers.

Microprobe evaluations revealed that the exposures led to chemical and phase alterations near the surface that extended beyond the oxide layers. This is illustrated in Figure 6, for an ME3 specimen exposed at 815 °C at 2,020 h. The recrystallized  $\gamma'$ -dissolution layer was depleted in Cr, Ti, Al, and Ta in comparison to the deep interior, due to the formation of the major oxides. Within 30  $\mu\text{m}$  of the oxidized



surface, the grain boundaries are depleted in Cr, Mo, Co and enriched in Ni relative to remote interior grain boundaries. Due to their high Cr, Mo, and Co content,  $M_{23}C_6$  carbides image brightly in back-scattered SEM (BSE) due to their high refractory content and primarily reside at the grain boundaries. More infrequent  $M_3B_2$  borides, enriched in Mo, Cr, and W, and MC carbides, enriched in Ti, Ta, and Nb, reside mostly within the grains (Ref. 7 and 12). The BSE image in Figure 6 shows a region extending in further than the precipitate-free zone is depleted in the bright  $M_{23}C_6$  carbides at the grain boundaries. For this exposure condition, at roughly 50  $\mu m$  depth there is a clear transition from negligible minor phase particle number density at the grain boundaries to full density. Near the surface, Cr from  $M_{23}C_6$  carbides and  $M_3B_2$  borides apparently diffused out to help sustain the  $Cr_2O_3$  scale growth, resulting in the local dissolution of these minor phases. Mo and Co also accumulated underneath the external scale in the  $\gamma'$ -dissolution layer. This resulted in adjacent superalloy grain boundaries that were depleted in Cr, Mo, and Co. The MC carbides appear to be stable during exposure and were present within the minor phase dissolution zone.

Tables 3 and 4 compare the thicknesses of the outer oxide scale, alumina finger penetration,  $\gamma'$ -dissolution layer, and the minor phase dissolution zone, for various exposure conditions of each alloy. Comparisons of the oxide scale thickness, alumina finger length, and  $\gamma'$ -dissolution layer for both alloys as functions of exposure time are shown in Figure 7. For ME3 (Ref. 7), invariant of time and temperature, the minor phase dissolution zone thickness was three times greater than that of the  $\gamma'$ -dissolution layer (where  $Al_2O_3$  fingers reside), which were roughly three times greater than the external oxide scale thicknesses. As these layer thicknesses are additive, for the most aggressive 815 °C at 2,020 h exposure imaged in Figure 6, removal of material to a depth of  $\sim 20 \mu m$  was necessary to eliminate both the external  $Cr_2O_3$ - $TiO_2$  scale and internal branched  $Al_2O_3$  fingers, while material removal to a depth of  $\sim 50 \mu m$  was necessary to eliminate the minor phase dissolution zone. Measurements for the mean oxide scale thickness and alumina finger length did not vary statistically between the two alloys for the majority of the exposure conditions, with the exception of 704 °C 100 h and 704 °C 440 h conditions. The mean  $\gamma'$ -dissolution layer thicknesses for LSHR showed agreement with ME3 for the 815 °C isotherm, however, showed slight differences for the 704 and 760 °C exposure conditions, possibly an indication of coupon-to-coupon variability.

## Effect of Exposures on Fatigue Life

### Uniform-Gage Fatigue of LSHR

Fatigue tests of uniform-gage specimens of LSHR were performed at 760 °C, with a maximum stress of 841 MPa and minimum stress of -428 MPa applied in all tests. Preliminary testing of LSHR had shown these cyclic stresses are typically stabilized values generated in strain-controlled tests at a total strain range of 0.76 percent and minimum/maximum strain ratio of 0. These preliminary tests were performed at a frequency of 0.5 Hz for 24 h, then continued at a higher frequency of 10 Hz. The short total test times and associated exposures encouraged internal- initiated failures at grain facets or non-metallic inclusions in tests at 704 and 760 °C, but surface initiated failures at 815 °C (Ref. 14). Such response has also been observed in ME3 (Ref. 15). The subsequent tests performed here on LSHR at 760 °C with the same applied stresses but a slower, constant frequency of 0.33 Hz, however, encouraged surface-initiated cracks to limit fatigue life, even for specimens without prior exposures. This testing temperature of 760 °C and frequency of 0.33 Hz allowed only minor surface oxidation during fatigue test durations of up to about 50 h, but this likely combined with cyclic relaxation of compressive residual stresses near the surface (Ref. 16) and was sufficient to typically result in surface-initiated failures.

The lives for fatigue tests of LSHR are compared in Table 5 and Figure 8. Stepwise linear regressions were performed on  $\log(\text{life})$ , using variables of temperature,  $\log(\text{time})$ , and their product. The resulting linear regression equation is given in Figure 9a, along with comparisons of estimated and actual lives. This equation indicated that increasing exposure temperature and increasing time reduced fatigue life. Their coefficients indicated they had comparable effects, when increased from minimum to maximum

settings employed here. The product of temperature and time also had a significant effect, indicating their effects were enhanced for combinations of high temperature and long time. This regression equation gave a fairly high coefficient of determination ( $R^2$ ) of about 0.87, but had a lack of fit that was significant at a probability of over 95%. As shown in Figure 9a, this lack of fit was evident at intermediate exposure conditions, where only small reductions in mean fatigue life were observed. Regressions of fatigue life versus depths of oxide scales, fingers, and dissolution zones each also had this problem of lack of fit, with poor agreement at intermediate exposure conditions. The coefficient of determination was not improved using any of these depths, or when using their sum. This is exemplified in Figure 9b, using the sum of oxide scales, fingers, and dissolution zones depths for a total depth of damage. Fatigue life decreased with increasing total depth of damage.

Fatigue lives for each condition were compared by one-way analyses of variance, and then grouped where no significant difference in life was observed. Exposures at 704 °C for 100 h gave no significant reduction in mean life for these limited tests, and could be grouped with unexposed specimens (Group N). However, longer exposures at 704 °C and exposures at higher temperatures significantly reduced mean fatigue life, at a statistical confidence of at least 95%. Specifically, exposures at 704 °C for 440 h and 2,020 h, 760 °C for 440 h, and 815 °C for 100 h, had comparable mean fatigue lives representing relatively low effects on life (Group L), about 50% of unexposed life. The mean lives for these different exposure conditions were statistically equivalent at a confidence of over 90% and significantly less than Group N fatigue life. But isothermal or cyclic exposures at 815 °C for 440 h produced significantly lower fatigue lives than Groups N or L. These conditions gave equivalent mean fatigue lives at a confidence of over 95% (Group M), and more severely reduced fatigue mean life to 20% of unexposed life. The highest reduction in mean fatigue life was observed for an exposure of 815 °C for 2,020 h (Group H), which reduced mean fatigue life by 98% or about 2% of the unexposed mean fatigue life.

Material blanks were also aged at 815 °C for 2,020 h before machining into specimens, to assess microstructure aging effects. These LSHR specimens had about 25% lower mean fatigue lives than unexposed specimens, at a statistical significance of over 95%. The data is plotted in Figure 8 for comparison. This reduction is likely due to reductions in strength, often observed after overaging (Fig. 3) of the strengthening  $\gamma'$  precipitates (Ref. 17). However, the fatigue lives of samples extracted from these aged blanks were significantly higher than for machined specimens that were tested after an exposure for the same duration and temperature.

Several specimens were subjected to cyclic exposures giving an accumulated time of 440 h at 815 °C, for comparison to specimens given static exposures of 440 h at 815 °C. The surfaces of fatigue specimens typically looked very similar after these two exposure conditions, although the outer oxide layers appeared to spall in several locations during cyclic exposure, Figure 10a and b. Energy-dispersive X-ray spectroscopy (EDS) indicated that the Cr-rich oxide layer spalled off in some locations, leaving the underlying  $\text{Al}_2\text{O}_3$ -rich layer uncovered. Nevertheless, corresponding mean fatigue lives of the isothermal and cyclic exposures were equivalent at a confidence of 95% (Group M, Fig. 8).

### **Notch Fatigue of ME3**

Fatigue tests of ME3 were performed on notch specimens at 704 °C. The stress concentration of the notch forced the failure initiations to remain at the surface, and did not allow internal crack initiation sites such as inclusions or large grains to limit life. The testing temperature was not expected to cause rapid surface changes during the fatigue test durations of up to about 50 h, based on the examinations of coupons exposed at 704 °C. This fatigue test condition could represent a disk feature such as a bolt hole or fillet for a service application near highest current disk temperatures.

The ME3 fatigue lives are compared in Table 6 and Figure 11. For unexposed and exposed conditions, fatigue life varied more for ME3 notched fatigue tests than for LSHR uniform gage fatigue specimens. This gave increased root mean square error in regression equations, but still allowed inspection of trends. Stepwise linear regression was again performed on log (life), using variables of temperature, log(time), and their product. The resulting linear regression equation is given in Figure 12a,

along with comparisons of lives estimated by the equation and actual lives. This equation again indicated that increasing temperature and time reduced fatigue life. Temperature had the strongest influence on fatigue life here, based on the higher magnitude of the coefficient for temperature than for time. The product of temperature and  $\log(\text{time})$  did not have a significant effect on life, indicating no significant enhancement for combinations of high temperature and high time as observed for LSHR uniform gage fatigue specimens. Regressions of fatigue life versus depths of oxide scales, fingers, dissolution zones, and their sum each did not give improved coefficients of determination or root mean square errors. This is illustrated in Figure 12b, again showing fatigue life decreased with total depth of damage.

As for uniform gage fatigue of LSHR, ME3 notch fatigue lives for each condition were compared by one-way analyses of variance, and then grouped where no significant difference in life was observed, Figure 11. After exposures at 704 °C for 100 h and 440 h, no significant reductions in mean life were identified with these limited notched fatigue tests. However, exposures of 704 °C for 2,020 h and those at 760 and 815 °C gave significantly lower mean life than unexposed specimens, at a statistical confidence of 95%. Yet, the exposure conditions of 704 °C for 2,020 h and 760 °C for 440 h appeared to be transitional, and gave more widely varied lives that spanned between multiple groups. These required comparisons of failure modes, to confirm the group classifications. The largest reduction in mean fatigue life was again observed for the exposure condition producing the largest surface layer thicknesses, 815 °C for 2,020 h, which reduced mean fatigue life by 99%. Also, specimens exposed at conditions giving comparable intermediate values of surface layer thicknesses, 704 °C for 2,020 h, 760 °C for 440 h, and 815 °C for 100 h, had statistically equivalent mean fatigue lives at a confidence of 95%. This indicated that fatigue life was related to the depth of environmental attack. However, as will be shown in failure mode evaluations, both crack initiation and crack growth modes were affected by the exposures.

Material blanks aged at exposure conditions of 815 °C for 440 h and 2,020 h and then machined into specimens (Table 6), as well as specimens exposed in vacuum at 815 °C for 440 h (Table 7), all had fatigue lives not significantly reduced from that of unexposed specimens. These results are included for comparison in Figure 11. Therefore, the debits in fatigue life associated with exposures for notched specimens were due to environmental attack, and not due to aging of the remote interior microstructure during pre-exposures. Several specimens were exposed at 815 °C for 2,020 h and then polished to remove only the outer oxide scales (20  $\mu\text{m}$ ), or all oxide scales and the minor phase dissolution zones (50  $\mu\text{m}$ ). For these samples, fatigue lives are also included in Figure 11. Polishing to a depth of 20  $\mu\text{m}$  only slightly improved fatigue life for this exposure condition, while removing 50  $\mu\text{m}$  restored life to unexposed levels.

The effects of exposure on fatigue lives of LSHR and ME3 could be compared by normalizing fatigue lives of exposed specimens by mean fatigue life of unexposed specimens, Figure 13. Notch fatigue life of ME3 appeared to be influenced more by exposures at intermediate temperatures and times than for uniform gage life of LSHR. This could be due to differences in how the fatigue lives of the varied materials, specimen configuration, and test conditions were influenced by intermediate exposures. Therefore, several notch fatigue configuration specimens were prepared from LSHR blanks, some exposed at an intermediate condition of 815 °C for 440 h, then all were fatigue tested at 704 °C using the same conditions as for the ME3 notched specimens. Unexposed LSHR specimens had about 35% higher notched fatigue life than for ME3 in these conditions, attributable to the finer LSHR grain size (Fig. 3). Nevertheless, the normalized mean fatigue life of exposed notch specimens of LSHR were reduced by this exposure just as for ME3, and did not appear to be alloy dependent, Figure 13b. This may be related to the concentration of stresses produced by the notch at the exposed surface. However, dissimilar failure modes could also be operative for the two alloys, and should to be compared.

## **Effect of Exposures on Fatigue Failure Modes**

### **Uniform-Gage Fatigue of LSHR**

Failure initiation modes of the LSHR tested specimens are compared in Figures 14 to 18. To gain further information of failure initiation modes, typical secondary cracks are also presented in the gage

sections of variously exposed specimens in Figure 19. Figures 14 to 17 show the failure modes of specimen failures were grouped according to failure mode and associated fatigue life, indicated as Groups N, L, M, and H in the fatigue life plot of Figure 8. For each unexposed specimen, usually one transgranular crack initiated at the specimen surface, normal to the loading axis, to cause failure, Figure 14. In some cases, these cracks initiated at angled faces of grains adjacent to the surface, but these shifted to transgranular crack growth within 10  $\mu\text{m}$  of the surface. These cracks then grew in a predominantly transgranular mode normal to the loading axis. This failure mode was also usually observed after exposures of 100 h at 704 °C, and could be grouped with unexposed specimens in showing no consistent change in failure mode or life (Group N).

However, for Group L specimens exposed at 704 °C for 440 h and 2,020 h, 760 °C for 440 h, and 815 °C for 100 h, consistent changes in failure mode were observed, Figure 15. For this group, more cracks were present in the oxide scales coating the sides of these specimens, Figure 19b to 19e. While shorter cracks were roughly normal to the loading axis, they sometimes joined to follow the boundaries of underlying grains. Usually, a singular failure initiation point was observed on each fracture surface as in Figure 15a, but occasionally multiple crack initiation points were observed, Figure 15b. The main crack became more torturous and mixed in mode, with several grain boundary surfaces evident adjacent to the cracked oxide scales of the specimen surface as shown in Figure 15, as indicated by rounded contours of grain boundaries and the rougher texture produced by coarser secondary  $\gamma'$  particles precipitating and growing along grain boundaries. However, these initial cracks at surface grain boundaries only grew to a depth of about 30  $\mu\text{m}$ , then transitioned to transgranular crack propagation through adjoining interior grains.

Group M specimens, subjected to a constant exposure for 440 h at 815 °C and cyclic exposure for a cumulative hot time of 440 h at 815 °C, had a more extended intergranular failure initiation mode, Figure 16. More frequent cracking of the outer oxide scales was observed, with a mixture of shorter cracks roughly normal to the loading axis, and longer cracks linked to follow the boundaries of underlying, unrecrystallized grains, Figure 19j and 19k. The main failure initiation point had grain boundaries exposed by intergranular crack growth to a depth of about 60  $\mu\text{m}$ , Figure 16. This was again followed by a transition to predominantly transgranular crack propagation further into the specimen interior. Their mean fatigue lives represented about 20% of unexposed mean fatigue life.

Finally, for the most severe exposure at 815 °C for 2,020 h of Group H specimens, extensive cracking of the oxide layers and adjoining recrystallized grains was evident on the specimens' sides (Fig. 19g) and along the fracture surfaces, Figure 17. Crack initiation and propagation of the adjoining unrecrystallized grains remained predominantly intergranular until final overload failure. This was associated with the highest effect on mean fatigue life of all tested conditions, with the 98% reduction giving about 2% of unexposed mean fatigue life. This indicated that both crack initiation and crack growth modes could be affected by the exposures, and explained why estimations of fatigue life assuming only enhanced crack initiation at oxide layers of varied depth were insufficient.

There were several exceptions to the above trends. One unexposed specimen, which failed from an aluminum oxide granulated inclusion at the specimen surface shown in Figure 18a, had a lower life than Group N specimens at a statistical confidence of over 95%, yet it exhibited transgranular crack initiation and growth. Previous work has shown that inclusions intersecting a disk superalloy specimen surface can inordinately reduce fatigue life, and this should be considered a separate failure mode whose probability of occurrence can depend on the inclusion number density, inclusion size, and surface area of the specimen gage section (Ref. 4), as well as the specimen surface and fatigue test conditions. Specimens aged as blanks at 815 °C for 2,020 h had lower mean life than Group N specimens, at a statistical confidence of over 95%, yet transgranular crack initiation and growth. One of these specimens failed from a near-surface pore (Fig. 18b), while another failed from an internal inclusion. However, three other specimens tested after short exposures at low temperatures had cracks initiating from internal inclusions, but no significant divergence in life from others at the same exposure condition. The lower life after aging the blanks could also be related to a reduction in strength brought on by extended coarsening of the  $\gamma'$  precipitates producing the changes evident in Figure 3.

Longitudinal metallographic sections were also prepared for selected failed specimens, to examine gage cross sections containing secondary surface cracks adjacent to the dominant failure initiation site, and are shown in Figure 20. These locations would be unloaded as the dominant crack grew, and not subjected to higher stresses often generated near final specimen failure. These locations were also observed before sectioning for comparisons, shown previously in Figure 19. As shown in Figure 19a, 19h and 20a, group N specimens had very few secondary cracks, which grew from the surface across grains roughly normal to the loading axis. Group L specimens had more frequent secondary cracks, Figure 19c through Figure 19e and Figure 20b. These were often still relatively flat and normal to the loading axis, initiating in the outer oxide layers. Secondary cracks for Group M specimens sometimes linked together to outline underlying grain boundaries, and then grew along grain boundaries for a short distance, as shown in Figure 19j and 19k. Finally Group H specimens had very many cracks in the recrystallized zone along the alumina fingers, Figure 20d. Some of these cracks then propagated as intergranular cracks extending into the specimen interior, evident on the section's adjacent fracture surface.

### **Notch Fatigue of ME3**

Failure initiation modes of ME3 in the notch fatigue tests at 704 °C are compared in Figure 21-24. All failures initiated from the notch surface. The dominant failure initiation modes could be divided into three groups of N, M, and H (Fig. 11) according to failure modes and fatigue lives, but their associations with exposure conditions were less rigid than for the uniform gage fatigue specimens. This could be due in part to the fact that a far smaller volume was highly stressed near the notch root for ME3, in comparison to that for the uniform gage section for LSHR. Therefore, representative images are presented to describe each group for ME3, rather than exposure condition.

Group N specimens failed from primary cracks initiating and propagating in a predominantly transgranular fashion through grains, with crack growth roughly normal to the loading axis, Figure 21. This most often occurred for unexposed specimens, and sometimes after exposures of 704 °C for 100 h, 440 h, and 2020 h. In some cases, cracks initiated at angled faces of grains adjacent to the surface, but these shifted to transgranular crack growth within 10 µm of the surface. Specimens failed from either one or two primary crack initiation points, indicated by the arrows in Figure 21. Fatigue life for these specimens remained within 28,326 to 100,256 cycles.

Group M specimens failed from primary cracks that started more torturous and mixed in mode, with several grain boundary surfaces evident adjacent to the cracked oxide scales of the specimen surface as shown in Figure 22. These initial cracks at surface grain boundaries usually only grew up to one grain deep, typically about 30 µm, then transitioned to transgranular crack propagation through grains further interior. This most often occurred for specimens exposed at 704 °C for 440 h and 2020 h, 704 °C for 440 h, and 815 °C for 100 h. With the thicker oxides generated by some exposures, fatigue encouraged a higher number of cracks along the notch surface than for Group N specimens, which produced more numerous crack initiation sites on the fracture surface. These surface cracks were similar to those of the uniform gage specimens, although restricted to the highly stressed notch root section. But this failure mode was also observed for one unexposed specimen and for one specimen exposed at 815 °C for 440 h, showing the mode was not dependent only on exposure condition and associated outer surface layers for notched specimens. Fatigue life for these specimens ranged from 2,430 to 30,472 cycles.

Group H specimens had extensive cracking across more expansive oxide layers and recrystallized grain zones along the notch surface and at many failure initiation sites on the fracture surfaces, as shown in Figure 23. Environmental exposures caused the adjacent unrecrystallized grains' boundaries to be degraded, leading to intergranular propagation that extended into the interior for several hundred microns. This failure mode was observed for exposures at 815 °C for 440 and 2,020 h. Fatigue life for these specimens ranged from 397 to 874 cycles.

Additional tests were performed with altered exposure and testing conditions, to further examine the relationships between fatigue life and failure modes, Table 7. ME3 notch specimens were exposed in vacuum at 815 °C for 440 h, and others were aged as blanks at exposure conditions of 815 °C for 440 h

and 2,020 h and then machined into specimens for testing. Their fatigue lives were not significantly reduced from that of unexposed specimens. This indicated the debits associated with exposures were due to environmental attack and that aging of the remote interior microstructure during pre-exposures did not significantly affect notch fatigue life in these test conditions. Yet, they had a different failure mode. After transgranular crack initiation as for unexposed specimens, crack propagation transitioned to become predominantly intergranular, as shown in Figure 24. An intergranular crack propagation mode was also observed for specimens exposed at 815 °C for 2,020 h and then re-polished to selectively remove surface layers, which will be discussed below. Long term aging of the internal microstructure at these conditions had apparently increased the potential for intergranular cracking during notch fatigue tests. It is not clear why this shift in crack propagation mode was not observed in tests of uniform gage LSHR specimens aged at 815 °C for 2,020 h, but this apparently was related to the different testing configuration and conditions.

Prior exposures at intermediate conditions of ME3 notch fatigue specimens appeared to have greater effects on fatigue life at 704 °C than for LSHR uniform gage fatigue specimens tested at 760 °C, shown in Figure 13a. However, several LSHR specimens machined into the notch fatigue specimen configuration, exposed at 815 °C for an intermediate time of 440 h, and tested at 704 °C had comparable normalized fatigue lives to ME3, Figure 13b. As shown in Figure 25b, LSHR notch fatigue specimens given this prior exposure had a very similar failure initiation mode as for ME3 specimens in Group H, with extensive cracking across the oxide layers and recrystallized grain zones along the notch surface, at many failure initiation sites. Intergranular propagation extended into the interior for 15 to 25  $\mu\text{m}$ , not nearly as deep as for ME3 specimens. But overall, this showed that notched specimens of both alloys fatigue tested at 704 °C had lives affected more by prior exposures at these intermediate conditions.

It is curious that aging at 815 °C for 2,020 h in the same furnace reduced fatigue life for LSHR uniform gage specimens, but did not consistently do so for ME3 notch specimens, Table 6. This could be due in part to the different coarsening response of the two alloys'  $\gamma'$  precipitates, Figure 3. After this extended aging, ME3 had significantly finer secondary  $\gamma'$  precipitates than LSHR, which could explain the smaller reductions in tensile strength. This also could be associated with the differing effects of aging-induced reductions in strength on uniform gage versus notched specimens. In the uniform gage of LSHR specimens, maximum cyclic stresses were maintained by the test control waveform, and reduced yield and ultimate strength could lower the fatigue stress-life response of aged specimens. But in the notches of ME3 specimens, maximum cyclic stresses of aged specimens could be reduced in comparison to those of unexposed specimens, due to more plastic flow in the notch. For the same applied net section stress, this would produce lower maximum cyclic stresses in the notch of aged specimens than for those without the extended aging. This could compensate for the lower fatigue stress-life response of aged specimens.

Longitudinal metallographic sections were also prepared across a primary failure initiation location for selected ME3 specimens, and are compared in Figure 26. As shown in Figure 26a, group N specimens had few, transgranular secondary cracks. Group M specimens had more numerous secondary cracks, which sometimes started at grain boundaries but became transgranular during crack growth, Figure 26b. As observed for uniform gage specimens, Group H specimens had very many cracks of the outer oxide scales and recrystallize zone, which usually grew along the alumina fingers, Figure 26c. Intergranular cracks sometimes then extended into the specimen interior.

### **Effects of Individual Exposed Surface Layers on Fatigue Failures in Notch Specimens**

The different surface layers had different compositions and phases, so could have different cracking properties. Therefore, the effects on fatigue life of individual surface layers generated by these exposures were examined, by polishing away selected surface layers before fatigue testing. These experiments were performed on ME3 notch fatigue specimens, in order to ensure all fatigue failures occurred at the polished notch surface. Samples given the extreme exposure condition of 815 °C for 2,020 h were studied here, as this exposure gave the largest dimensions of layers and consistently gave the Group H failure mode.

Polishing away material to a total depth of 20  $\mu\text{m}$  removed the outer  $\text{Cr}_2\text{O}_3$ - $\text{TiO}_2$  scale plus inner  $\text{Al}_2\text{O}_3$  branched fingers. However, this gave only marginally improved fatigue life, to an average of 1,305 cycles, included for comparison in Figure 11. Fractographic evaluation revealed that the specimens failed by multiple intergranular crack initiations, with the cracks continuing to propagate along grain boundaries into the interior, Figure 27a. This life and failure mode remained consistent with that of Group H specimens.

Polishing away more material to a total depth of about 50  $\mu\text{m}$  removed the above layers and also the minor phase dissolution zone. This gave a significant increase in mean fatigue life to 35,998 cycles, which is nearly comparable to the mean fatigue life of the unexposed specimens, Figure 11. Furthermore, a single, transgranular crack initiated failure, Fig 27b, which is typical of unexposed failures. These aspects of fatigue life and crack initiation mode were consistent with Group N specimens. However, the deeply polished specimens had intergranular propagation extending over 1 mm in distance before overload. This crack propagation mode was consistent with Group H ME3 specimens. It would appear the deeper intergranular crack propagation mode was clearly related to aging of the internal microstructure during this exposure, as shown for specimens exposed in vacuum and blanks aged at 815 °C for 440 to 2,020 h before machining into specimens.

### Effects of Exposures on Tensile Response

Slow strain rate tensile tests described in ASTM G129-00 have often been used to screen the effects of dynamic environment-assisted cracking. But the standard indicates these tests have also been successfully used to screen for embrittlement due to prior hydrogen charging and plating processes. Therefore, tensile tests of varied displacement rates and corresponding strain rates were performed after exposures of LSHR and ME3, to examine exposure effects on tensile strength and ductility.

LSHR tensile specimens were exposed in air at 704 °C for 2,020 h, 760 °C for 440 h, and 815 °C for 2,020 h, along with blanks that were later machined into specimens. Typical tensile stress-strain curves are shown in Figure 28a for tests at 760 °C performed with a displacement rate of 0.1041 mm/s and average strain rate of  $5.0 \times 10^{-3} \text{ s}^{-1}$ , approximating the rates present for the fatigue tests. Companion tensile tests of LSHR performed at 704 °C with a much slower displacement rate of 0.0017 mm/s are compared in Figure 28b. Measured ultimate tensile strength and inelastic strain at fracture are listed in Table 8. Strengths were not strongly affected by the exposures at 704 and 760 °C. However, the exposure of 815 °C for 2,020 h reduced tensile strength by 150 to 190 MPa in the tensile tests, with greater effects observed for the slow strain rate testing condition. Yet, blanks exposed 815 °C for 2,020 h and subsequently machined into specimens produced comparable strengths for those given equivalent exposures in air. This indicated reductions in strength were primarily due to aging of the overall microstructure, and is consistent with the lower fatigue life observed for LSHR blanks aged at these conditions.

Ductility, as indicated by inelastic fracture strain, was reduced by exposures, going from 14 to 20% in unexposed specimens to as low as 1.9 to 4.2% for specimens exposed 815 °C for 2,020 h. Greater reductions in ductility were observed in tests at the slower strain rate. This suggested that slow strain rate tensile tests could be useful for screening exposure effects. On the other hand, blanks exposed at 704, 760 and 815 °C all had higher ductilities than unexposed specimens, at both fast and slow strain rate conditions. This indicated the reductions in ductility were driven by prior exposures in air, not aging of the overall microstructure.

Several tensile tests of ME3 were performed in air at 704 °C with a displacement rate of 0.0017 mm/s, just as for LSHR. The response and effects of prior exposure or blank aging of 815 °C for 2,020 h were quite comparable to LSHR, Figure 28b. Therefore, most tensile tests of ME3 were performed at 704 °C in a vacuum pressure not exceeding  $8 \times 10^{-6}$  torr, to assess the effects of prior exposures in air without the influence of an air environment during the tensile test, Table 9. Typical tensile stress-strain curves are shown in Figure 29, for displacement rates of 0.017 mm/s and 0.0017 mm/s. Ultimate tensile strength and inelastic strain at fracture are compared in Table 9 and Figure 29. Tensile strength was not

reduced in tensile tests by exposure of 2,020 h at 704 °C, but was reduced about 80 MPa by exposure of 2,020 h at 815 °C. Unlike tests in air, ductility was only moderately reduced by prior exposures for tensile tests performed in vacuum, going from 22 to 25% in unexposed specimens to 18 to 19% in specimens exposed 2,020 h at 815 °C. So exposure effects on ductility were clearly more acute in air. The slower strain rate decreased ultimate strength by 150 to 200 MPa, for each specimen exposure condition.

Several ME3 specimens were again re-polished after exposure, to remove the external oxide and oxide subscale from the gage surface (20 µm depth removed), and these showed a small improvement in tensile ductility. However, removal of all discussed layers including the minor phase dissolution zone, (50 µm depth removed), gave a full recovery in tensile ductility for each strain rate. These re-polished specimens still had tensile strengths reduced about 80 to 100 MPa (Table 9) from unexposed specimens, so the strength reductions were confirmed to be due to extended aging of the interior microstructure. Therefore, while ductility was reduced by the surface zones produced by exposures in air, strength was reduced in both LSHR and ME3 by extended aging of the interior microstructure, Figure 3.

Typical tensile fracture surfaces are compared in Figure 30. LSHR specimens exposed at 815 °C for 2,020 h and tested in air at 704 and 760 °C had very many surface cracks initiated at the outer oxide layers and then grown by intergranular cracking through the minor phase depleted zone and underlying superalloy. ME3 specimens exposed at the same conditions in air and tested in vacuum at 704 °C also had very many surface cracks initiated in the oxide layers, with subsequent intergranular cracking through the minor phase depleted zone. However, the underlying ME3 superalloy failed by transgranular microvoid coalescence. Additional exposed ME3 specimens which were polished to remove the outer oxide layers and minor phase depleted zone also failed by transgranular microvoid coalescence. This indicated that the intergranular cracking observed for exposed as well as aged specimens required an air environment, and appeared related to an increased environment susceptibility of aged grain boundaries.

## Summary and Conclusions

The effects of high temperature exposures in air on the microstructure and fatigue properties of two powder metal disk superalloys were determined. Fully machined mechanical test specimens of LSHR and ME3 were exposed at 704, 760, and 815 °C, for times up to 2,020 h. Coupons and blanks of both alloys were also exposed at the same conditions prior to machining to isolate the effect of the aging treatment on microstructures and fatigue properties. The depths of environmental attack were measured for each case. Uniform gage and notch gage fatigue tests were performed at 704 and 760 °C, for selected exposure conditions.

Fatigue resistance was reduced up to 98% in both superalloys by selected exposures. This was associated with enhanced cracking of surface oxide layers, followed by cracking of underlying grain boundaries depleted of minor phases, which then continued further into the interior. Tensile tests were subsequently performed to further investigate effects of the exposures on tensile response in air and in vacuum. The exposures reduced strength due to aging of the internal microstructure, and reduced ductility due to the enhanced cracking of surface layers. But intergranular cracking of the underlying superalloy was suppressed for tensile tests in vacuum. The effects of exposures on fatigue life, tensile strength, and tensile ductility were compared. The associated failure modes and their relationships to exposure-induced changes in compositions and phases near the surface were determined.

It can be concluded from this work that:

- 1) Extended exposures on machined specimens in air at high temperatures can produce surface oxide layers and oxidation-effected zones with enhanced susceptibility to cracking.
- 2) This can result in significantly lower fatigue lives, strength, and ductility for disk applications exposed at these conditions, in uniform sections and more acutely at notches.
- 3) Exposures can also produce aged microstructures having reduced strength and higher susceptibility to environment-assisted intergranular cracking in air.



- 4) Such aged microstructures can still have fatigue lives and ductilities near that of unaged specimens.
- 5) Cyclic exposures for equivalent cumulative times at temperatures up to 815 °C do not accelerate this damage.
- 6) Service exposure limits of temperatures below 704 °C and times below 440 h could be needed in some disk applications to prevent these effects, as longer exposures near 704 °C or higher temperature exposures can substantially degrade fatigue lives and ductility without effective environmental barrier coatings.

## References

1. Furrer, D., Fecht, H., "Ni-based Superalloys for Turbine Discs," *J. Metals*, V. 51, No. 1, 1999, pp. 14-17.
2. S. D. Antolovich, P. Domas, J. L. Strudel, "Low Cycle Fatigue of Rene' 80 as Affected by Prior Exposure," *Met. Trans. A*, V. 10A, 1979, pp. 1859-1868.
3. T. P. Gabb, J. Telesman, P. T. Kantzos, J. W. Smith, "Effects of High Temperature Exposures on Fatigue Life of Disk Superalloys," *Superalloys 2004*, ed. K. A. Green, H. Harada, T. E. Howson, T. M. Pollock, R. C. Reed, J. J. Schirra, S. Walston, The Minerals, Metals, and Materials Society (TMS), Warrendale, PA, 2004, pp. 269-274.
4. D. R. Chang, D. D. Krueger, R. A. Sprague, "Superalloy Powder Processing, Properties and Turbine Disk Applications," *Superalloys 1984: Proceedings of the 5<sup>th</sup> International Symposium on Superalloys*, ed. M. Gell, C. S. Kortovich, R. H. Bricknell, W. B. Kent, J. F. Radavich, TMS, Warrendale, PA, 1984, pp. 245-273.
5. D. A. Woodford, "Gas Phase Embrittlement and Time Dependent Cracking of Nickel Based Superalloys," *Energy Materials: Materials Science and Engineering for Energy Systems*, V. 1, No. 1, March 2006, pp. 59-79.
6. A. Encinas-Oropesa, G. L. Drew, M. C. Hardy, A. J. Leggett, J. R. Nicholls, N. J. Simms, "Effects of Oxidation and Hot Corrosion in a Nickel Disc Alloy," *Superalloys 2008: Proceedings of the 11<sup>th</sup> International Symposium on Superalloys*, ed. R. C. Reed, K. A. Green, P. Caron, T. P. Gabb, M. G. Fahrman, E. S. Huron, S. A. Woodard, TMS, Warrendale, PA, 2008, pp. 609-618.
7. C. Sudbrack, S. Draper, T. Gorman, J. Telesman, T. Gabb, D. Hull, "Oxidation and the Effects of High Temperature Exposures on Notched Fatigue Life of an Advanced Powder Metallurgy Disk Superalloy," *Superalloys 2012: 12<sup>th</sup> International Symposium on Superalloys*, ed. E. S. Huron, R. C. Reed, M. C. Hardy, M. J. Mills, R. E. Montero, P. D. Portella, J. Telesman, TMS, Warrendale, PA, 2012, pp. 863-872.
8. T. P. Gabb, J. Gayda, J. Telesman, P. T. Kantzos, "Thermal and Mechanical Property Characterization of the Advanced Disk Alloy LSHR," NASA/TM—2005-213645, Washington, D.C., June 2005. Telesman, *Superalloys 2012*
9. J. Telesman, T. Gabb, Y. Yamada, L. Ghosn, D. Hornbach, N. Jayaraman, "Dwell Notch Low Cycle Fatigue Behavior of a Powder Metallurgy Nickel Disk Alloy," *Superalloys 2012: 12<sup>th</sup> International Symposium on Superalloys*, ed. E. S. Huron, R. C. Reed, M. C. Hardy, M. J. Mills, R. E. Montero, P. D. Portella, J. Telesman, TMS, Warrendale, PA, 2012, pp. 853-862
10. JMP 11 Documentation Library, JMP, A Business Unit of SAS, Cary, NC, 2013.
11. T. P. Gabb, A. Garg, D. L. Ellis, K. M. O'Connor, "Detailed Microstructural Characterization of the Disk Alloy ME3," NASA/TM-2004-213066, Washington, D.C., May, 2004.
12. H. Jou, G. Olson, T. Gabb, A. Garg, D. Miller, "Characterization and Computational Modeling of Minor Precipitate Phases in Alloy LSHR," *Superalloys 2012: 12<sup>th</sup> International Symposium on Superalloys*, ed. E. S. Huron, R. C. Reed, M. C. Hardy, M. J. Mills, R. E. Montero, P. D. Portella, J. Telesman, TMS, Warrendale, PA, 2012, pp. 893-902.
13. Y. Y. Qiu, "Coarsening Kinetics of  $\gamma'$  Precipitates in Ni-Al and Ni-Al-Mo Alloys," *J. Mat. Sci.*, V. 31, 1996, pp. 4311-4319.

14. T. P. Gabb, R. A. MacKay, S. L. Draper, C. K. Sudbrack, M. V. Nathal, "The Mechanical Properties of Candidate Superalloys for a Hybrid Turbine Disk," NASA/TM—2013-217901, Washington, D.C., 2013.
15. T. P. Gabb, J. Telesman, P. T. Kantzos, A. Garg, "Effects of Temperature on Failure Modes for a Nickel-Base Disk Superalloy," *J. Failure Analysis and Prevention*, V. 7, Feb. 2007, pp. 56-65.
16. W. Zhang, G. R. Halford, "Investigation of Residual Stress Relaxation Under Cyclic Load," *Int. J. Fat.*, V. 23, 2001, pp. S31-S37.
17. R. F. Decker, "Strengthening Mechanisms in Nickel-Base Superalloys," *Proceedings on Symposium: Steel-Strengthening Mechanisms*, Zurich, Switzerland, Climax Molybdenum Company, 1969, pp. 147-170.

Table 1. Measured compositions in weight percent of tested materials.

Alloy - wt. %	Al	B	C	Co	Cr	Fe	Mo	Ni	Nb	Ta	Ti	V	W	Zr
LSHR	3.54	0.027	0.045	20.4	12.3	0.1	2.71	Bal.	1.49	1.52	3.45	0.0055	4.28	0.049
ME3	3.40	0.025	0.050	20.7	12.8	–	3.80	Bal.	0.90	2.30	3.70	–	2.00	0.05

Table 2. Summary of linear intercept grain size and precipitate dimensions for test materials.

		Secondary $\gamma'$						Tertiary $\gamma'$					
	Mean Linear Intercept Grain Size $\mu\text{m}$	Count -n	Median Area - $\mu\text{m}^2$	Mean $\gamma'$ Area $\pm$ 95% Conf. Interval - $\mu\text{m}^2$	Median $\gamma'$ Equiv. Radius - $\mu\text{m}$	Mean $\gamma'$ Equiv. Radius $\pm$ 95% Conf. Interval - $\mu\text{m}$		Count -n	Median $\gamma'$ Area - $\text{nm}^2$	Mean $\gamma'$ Area $\pm$ 95% Conf. Interval - $\text{nm}^2$	Median $\gamma'$ Equiv. Radius -nm	Mean $\gamma'$ Equiv. Radius $\pm$ 95% Conf. Interval -nm	
Alloy													
LSHR	15	204	0.051	0.051 $\pm$ 0.003	0.128	0.124 $\pm$ 0.004		119	678	761.2 $\pm$ 77.0	14.7	15.1 $\pm$ 0.7	
LSHR Aged 815 °C-2,020 h	15	200	0.077	0.079 $\pm$ 0.005	0.157	0.154 $\pm$ 0.006		0					
ME3	29	168	0.082	0.095 $\pm$ 0.011	0.162	0.161 $\pm$ 0.010		118	941.8	1283.0 $\pm$ 184.1	17.3	18.8 $\pm$ 1.3	
ME3 Aged 815 °C-2,020 h	29	191	0.044	0.049 $\pm$ 0.004	0.118	0.120 $\pm$ 0.005		0					

Table 3. Thickness of layers developed near the surface after exposures of ME3 in air. Oxide scale measurements were log-normally distributed, while the finger depths and  $\gamma'$ -dissolution layer thicknesses were normally distributed. The standard errors were determined by the variation in average values of the three areas.

Temperature - °C	Time (hour)	Mean Oxide Scale Thickness - $\mu\text{m}$ (Log normal)	Estimated Standard Error - $\mu\text{m}$	Mean Finger Depth - $\mu\text{m}$ (Normal)	Estimated Standard Error - $\mu\text{m}$	Mean $\gamma'$ -Dissolution Layer Thickness - $\mu\text{m}$ (Normal)	Estimated Standard Error - $\mu\text{m}$	Mean Carbide Dissolution Layer Thickness- $\mu\text{m}$	Standard Deviation - $\mu\text{m}$
704	10	0.185	0.035	0.164	0.060	ND	–	–	–
704	100	0.372	0.040	0.421	0.034	0.571	0.461	–	–
704	440	0.556	0.146	1.450	0.434	2.074	0.715	–	–
704	1010	0.927	0.046	2.343	0.872	2.732	0.256	–	–
704	2020	1.340	0.108	2.971	0.382	3.109	0.764	9.6	2.3
760	10	0.288	0.069	0.492	0.074	0.287	0.233	–	–
760	100	0.670	0.027	1.230	0.035	1.819	0.194	–	–
760	440	1.093	0.178	2.653	0.605	3.274	0.183	–	–
760	1010	1.457	0.140	3.830	0.437	4.232	0.616	–	–
760	2020	1.985	0.210	5.173	0.152	5.804	0.907	16.4	2.4
815	10	0.571	0.041	0.953	0.143	1.355	0.294	–	–
815	100	1.192	0.045	2.448	0.474	3.441	0.467	–	–
815	440	1.886	0.243	5.715	0.352	5.649	0.805	–	–
815	1010	2.662	0.125	7.235	0.245	7.845	0.291	–	–
815	2020	3.770	0.161	9.965	0.251	10.584	0.412	32.6	4.2

Table 4. Thickness of layers developed near the surface after exposures of LSHR in air. Oxide scale measurements were log-normally distributed, while the finger depths and  $\gamma'$ -dissolution layer thicknesses were normally distributed. The standard errors were determined by the variation in average values of the three areas.

Temperature - °C	Time (hour)	Mean Oxide Scale Thickness - $\mu\text{m}$ (Log normal)	Estimated Standard Error - $\mu\text{m}$	Mean Finger Depth - $\mu\text{m}$ (Normal)	Estimated Standard Error - $\mu\text{m}$	Mean $\gamma'$ -Dissolution Layer Thickness - $\mu\text{m}$ (Normal)	Estimated Standard Error - $\mu\text{m}$
704	100	0.126	0.069	0.150	0.032	0.554	0.089
704	440	0.428	0.116	0.613	0.242	0.979	0.230
704	2020	0.929	0.106	2.680	0.502	5.003	0.180
760	440	1.261	0.070	2.649	0.408	4.828	0.167
815	100	1.428	0.055	3.666	0.345	4.561	0.177
815	440	1.850	0.175	5.441	0.884	6.370	0.712
815	2020	3.883	0.531	9.816	0.385	13.480	1.185

Table 5. Summary of uniform gage fatigue test results at 760 °C for LSHR.

Specimen Identification	Prior Exposure Temperature -C	Prior Exposure Time -h	Life -cycles
<b>T3-L12</b>			<b>22,257*</b>
U3-L1			46,025
Z6-L14			49,879
T3-L17			55,123
T3-L15	Blank Aged 815C	2020	36,481
Z6-L17	Blank Aged 815C	2020	36,482
Z6-L18	Blank Aged 815C	2020	30,914
T3-L1	704	100	41,624
T3-L16	704	100	43,577
Z6-L11	704	100	45,108
T3-L2	704	440	25,734
Z6-L5	704	440	40,474
Z6-L16	704	440	33,584
T3-L4	704	2020	39,050
T3-L13	704	2020	39,831
Z6-L9	704	2020	16,896
T3-L11	760	440	43,119
Z6-L6	760	440	36,835
Z6-L15	760	440	33,222
T3-L5	815	100	25,894
T3-L8	815	100	23,036
Z6-L1	815	100	31,138
T3-L10	815	440	5,417
Z6-L4	815	440	11,921
Z6-L7	815	440	9,593
T3-L7	815	2020	669
T3-L14	815	2020	635
Z6-L2	815	2020	1,695
T3-L3	815	440 cyclic	9,186
T3-L9	815	440 cyclic	16,172
Z6-L8	815	440 cyclic	13,762
Z6-L10	815	440 cyclic	6,973

\* Premature failure at surface inclusion

Table 6. Summary of notch gage fatigue test results at 704 °C for ME3.

Specimen Identification	Prior Exposure Temperature - °C	Prior Exposure Time -h	Prior Exposure Environment	Fatigue Life - cycles
H111-NNR4				84,588
H101-NNR4				47,394
H111-NKR2				19,516
S101C-NER3				28,326
S101A -NER1	Blank Aged 815	440	Air	65,613
S101A-NEW1	Blank Aged 815	2020	Air	71,480
S101A-NER4	704	100	Air	100,256
S101C-NER8	704	100	Air	47,108
S101C-NEW5	704	100	Air	23,562
S101A-NER9	704	440	Air	4,531
S101A-NEW3	704	440	Air	33,730
S101B-NER3	704	440	Air	41,064
S101B-NEW6	704	440	Air	39,712
S101A-NER7	704	2020	Air	6,028
S101A-NEW2	704	2020	Air	15,265
S101B-NER5	704	2020	Air	31,150
S101B-NER9	704	2020	Air	4,810
S101B-NER6	760	440	Air	4,355
S101C-NER5	760	440	Air	30,472
S101C-NEW3	760	440	Air	8,422
S101B-NEW2	815	100	Air	10,284
S101B-NEW5	815	100	Air	6,002
S101C-NER9	815	100	Air	3,160
H101-NKR5	815	440	Air	874
H101-NNR5	815	440	Air	796
S101A-NER5	815	440	Air	2,430
H101-NKR2	815	2020	Air	397
H101-NLR1	815	2020	Air	482
S101A-NER3	815	2020	Air	588



Table 7. Summary of additional notch gage fatigue test results at 704 °C for ME3.

Specimen Identification	Prior Exposure Temperature - °C	Prior Exposure Time -h	Prior Exposure Environment	Notch Depth Removed - $\mu m$	Fatigue Life -cycles
S101A-NEW5	815	440	Vac		53,309
S101B-NER7	815	440	Vac		62,520
S101A-NER6	815	2020	Air	23	927
S101B-NER2	815	2020	Air	19	1,943
S101B-NER8	815	2020	Air	19	1,046
S101A-NER8	815	2020	Air	48	32,980
S101B-NER4	815	2020	Air	52	42,140
S101B-NEW3	815	2020	Air	52	32,873

Table 8. Summary of tensile test results at 704 °C and 760 °C in air for LSHR and ME3.

Alloy	Specimen Identification	Prior Exposure Temperature -C	Prior Exposure Time -h	Test Temperature -C	Test Environment	Displacement Rate - mm/s	Average Strain Rate -s <sup>-1</sup>	Yield Strength - MPa	Ultimate Strength -MPa	Inelastic Fracture Strain - %
LSHR	T3-T1A	None		704	Air	0.00173	8.3E-05	1057	1220	14.4
LSHR	T2-T5	None		704	Air	0.00173	8.3E-05	1028	1310	14.3
LSHR	T3-T2B	Blank 704	2,020	704	Air	0.00173	8.3E-05	1052	1197	22.1
LSHR	T3-T1C	704	2,020	704	Air	0.00173	8.3E-05	1062	1212	11.1
LSHR	Z6-T4B	Blank 760	440	704	Air	0.00173	8.3E-05	1009	1173	23.5
LSHR	T3-T4C	760	440	704	Air	0.00173	8.3E-05	1018	1182	12.2
LSHR	Z6-T1D	Blank 815	2,020	704	Air	0.00173	8.3E-05	948	1125	22.9
LSHR	T3-T1B	815	2,020	704	Air	0.00173	8.3E-05	912	1077	1.9
LSHR	T3-T4A	None		760	Air	0.104	5.0E-03	1038	1282	20.5
LSHR	T2-T3	None		760	Air	0.104	5.0E-03	1020	1284	17.7
LSHR	T3-T2A	Blank 704	2,020	760	Air	0.104	5.0E-03	1029	1281	25.0
LSHR	Z6-T3B	704	2,020	760	Air	0.104	5.0E-03	1034	1262	15.2
LSHR	Z6-T4D	Blank 760	440	760	Air	0.104	5.0E-03	993	1257	24.7
LSHR	Z6-T2B	760	440	760	Air	0.104	5.0E-03	1001	1248	16.1
LSHR	Z6-T1A	Blank 815	2,020	760	Air	0.104	5.0E-03	902	1186	23.2
LSHR	Z6-T2A	815	2,020	760	Air	0.104	5.0E-03	903	1137	4.2
ME3	H111-SRR1	None		704	Air	0.00173	8.3E-05	1031	1188	15.4
ME3	S101-SRW3	None		704	Air	0.00173	8.3E-05	1018	1180	18.0
ME3	S101-R1ANB	Blank 815	2,020	704	Air	0.00173	8.3E-05	870	1078	19.9
ME3	S101-R1ANC	Blank 815	2,020	704	Air	0.00173	8.3E-05	845	1043	25.3
ME3	H111-SRR3	815	2,020	704	Air	0.00173	8.3E-05	880	1000	2.1
ME3	H111-SRW5	815	2,020	704	Air	0.00173	8.3E-05	878	999	3.4

Table 9. Summary of tensile test results at 704 °C in vacuum for ME3.

Specimen Identification	Prior Exposure Temperature -C	Prior Exposure Time -h	Gage Depth Removed - $\mu$ m	Test Temperature -C	Displacement Rate -mm/s	Average Strain Rate -s <sup>-1</sup>	Yield Strength -MPa	Ultimate Strength -MPa	Inelastic Fracture Strain - %
S101-SRR1	None			704	0.00173	8.3E-05	1048	1128	22.8
S101-SRR3	None			704	0.00173	8.3E-05	1022	1145	21.9
S101-R94	704	2,020		704	0.00173	8.3E-05	1032	1118	26.3
S101-R61	815	2,020		704	0.00173	8.3E-05	960	1054	18.1
S101-R92	815	2,020	15	704	0.00173	8.3E-05	967	1058	19.6
S101-R91	815	2,020	66	704	0.00173	8.3E-05	963	1060	21.7
S101-SRR2	None			704	0.0173	8.3E-04	1027	1307	24.9
H101-SRW1	None			704	0.0173	8.3E-04	1032	1281	22.8
S101-R64	704	2,020		704	0.0173	8.3E-04	1015	1282	27.5
S101-R31	815	2,020		704	0.0173	8.3E-04	947	1209	19.5
S101-R32	815	2,020	15	704	0.0173	8.3E-04	988	1246	20.5
S101-R62	815	2,020	49	704	0.0173	8.3E-04	938	1225	30.3

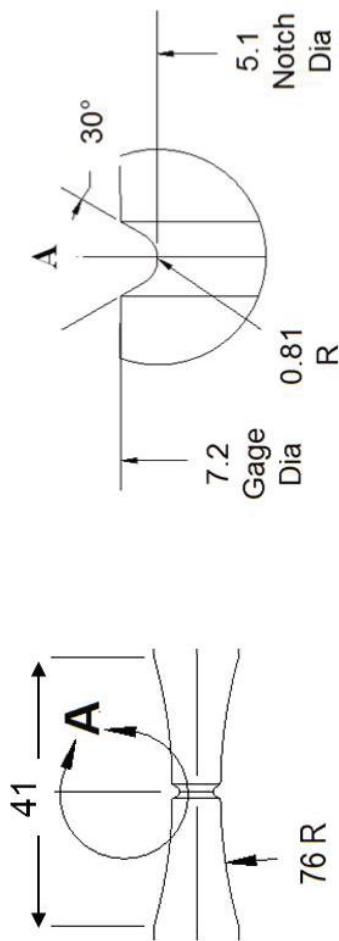


Fig. 1. Notch configuration for fatigue specimens of ME3, dimensions in mm.

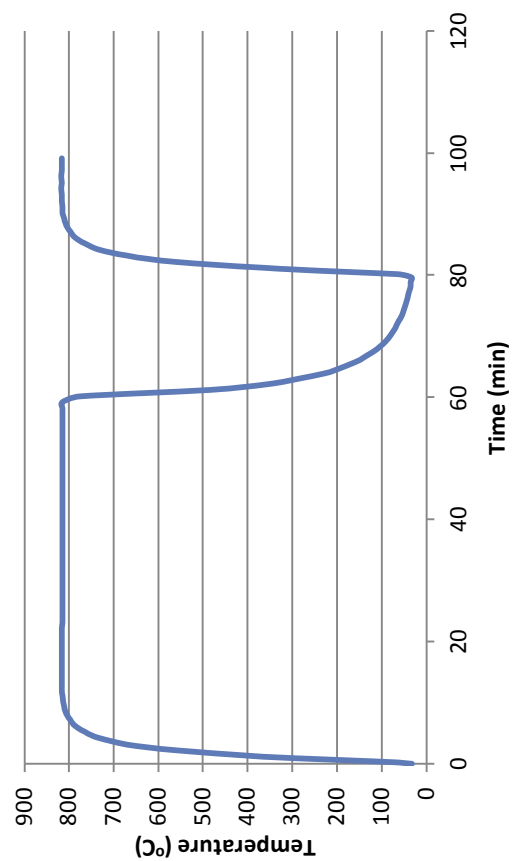


Fig. 2. Typical temperature versus time cycle for cyclic exposure of selected LSHR fatigue specimens, attaining maximum temperature of 815 °C for cumulative time of 440 h.

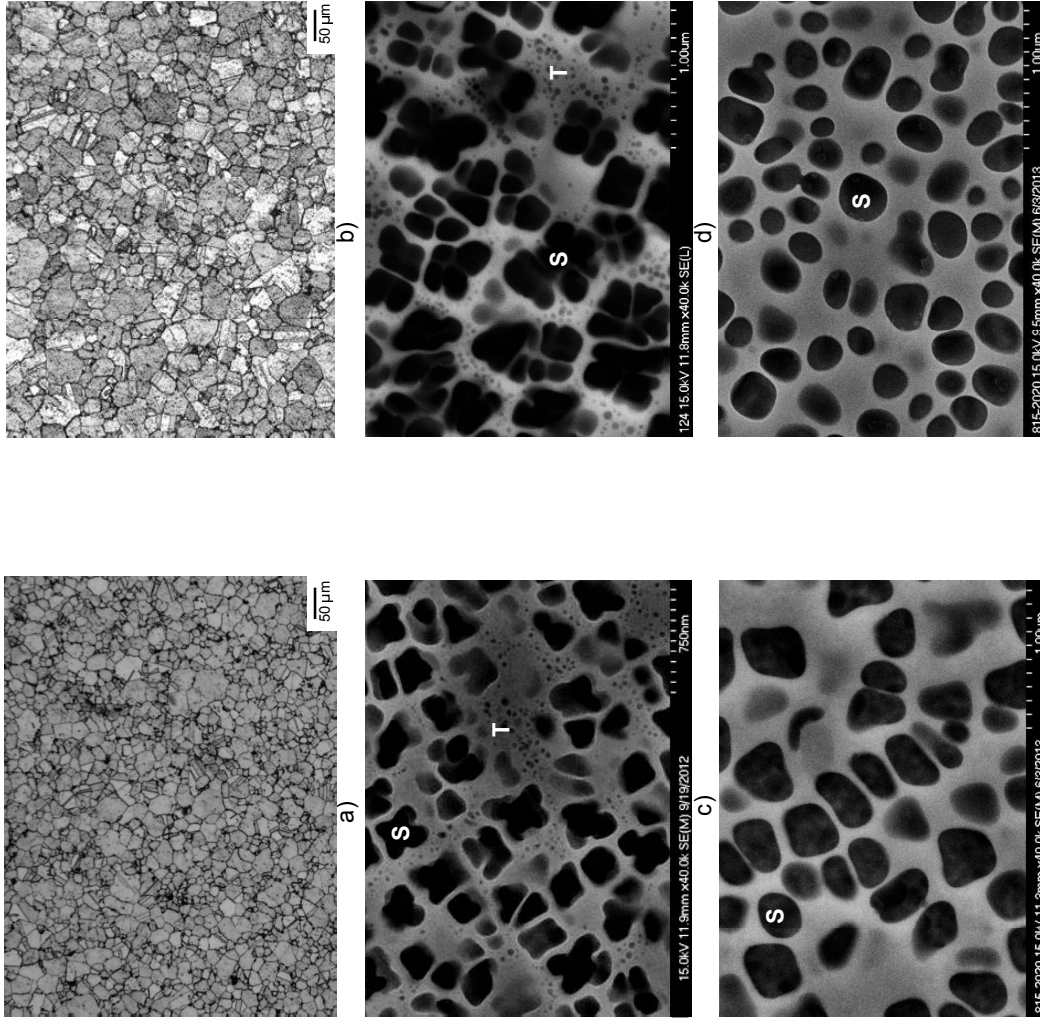


Fig. 3. Microstructures of the test materials: a) Optical microscope (OM) image of LSHR grain structure, b) OM image of ME3 grain structure, c) Secondary electron (SE) image of LSHR secondary (S) and tertiary (T) precipitates before aging or exposures, d) SE image of ME3  $\gamma'$  precipitates before aging or exposures, e) SE image of LSHR  $\gamma'$  precipitates after aging 815 °C for 2,020 h, f) SE image of ME3  $\gamma'$  precipitates after aging 815 °C for 2,020 h.

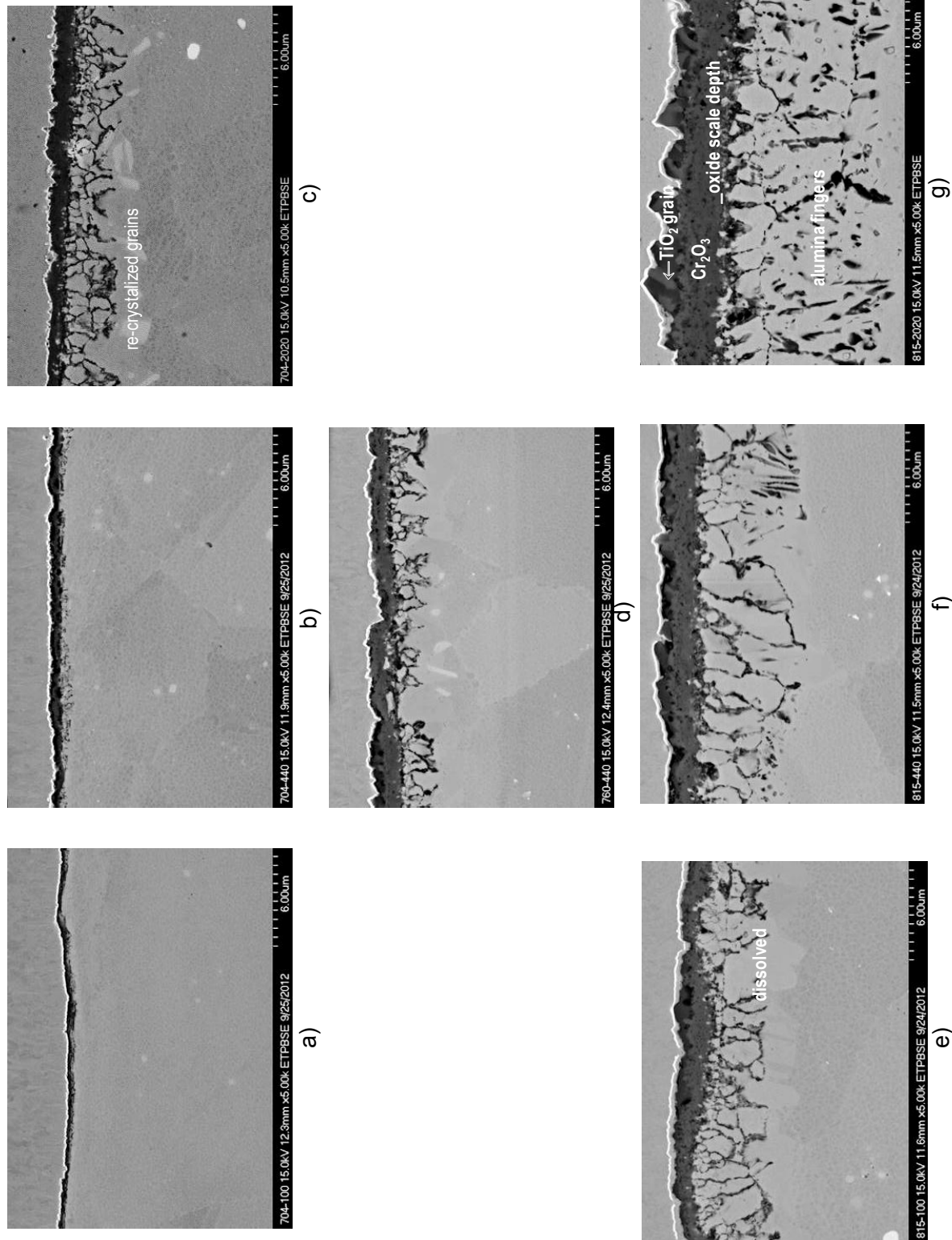


Fig. 4. Backscattered electron (BSE) images showing effects of prior exposures on LSHR surface microstructure (before testing): a) 704 °C-100 h., b) 704 °C-440 h, c) 704 °C-2,020 h, d) 760 °C-440 h, e) 815 °C-100 h, f) 815 °C-440 h, g) 815 °C-2,020 h.

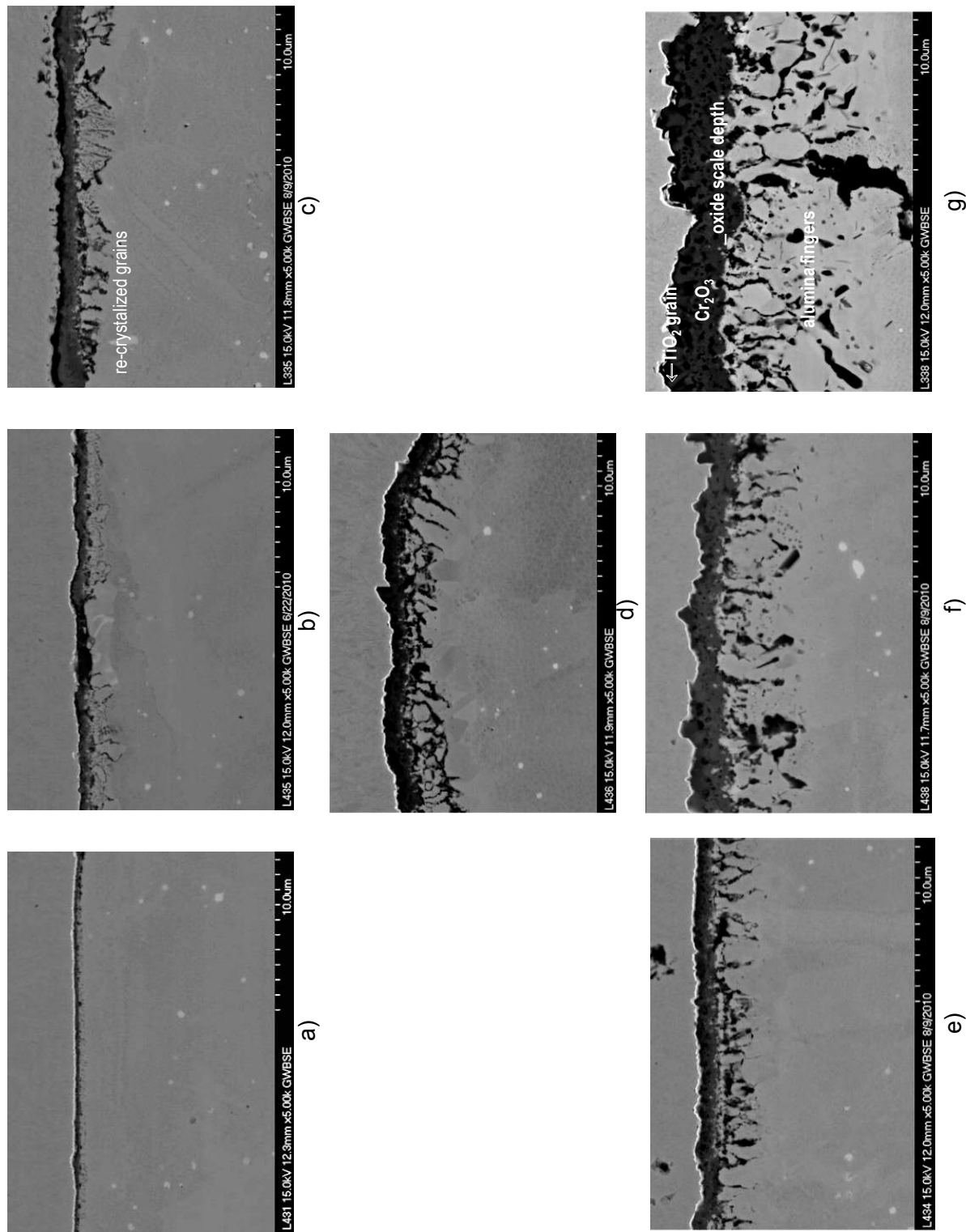


Fig. 5. BSE images showing effects of prior exposures on ME3 surface microstructure: a) 704 °C-100 h, b) 704 °C-440 h, c) 704 °C-2,020 h, d) 760 °C-100 h, e) 815 °C-100 h, f) 815 °C-440 h, g) 815 °C-2,020 h.



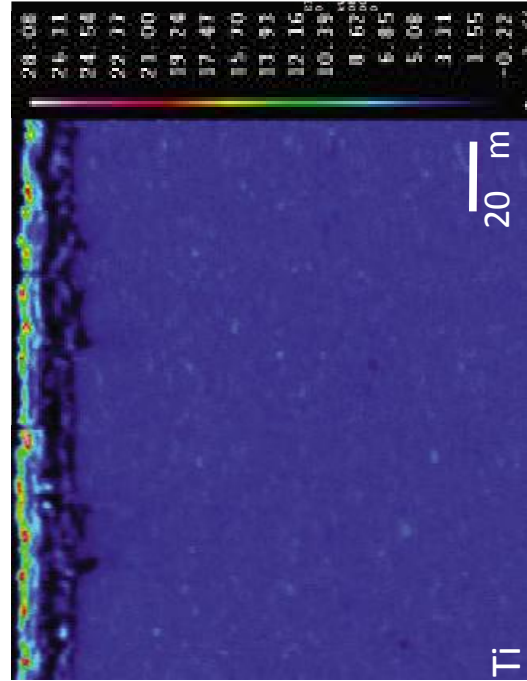
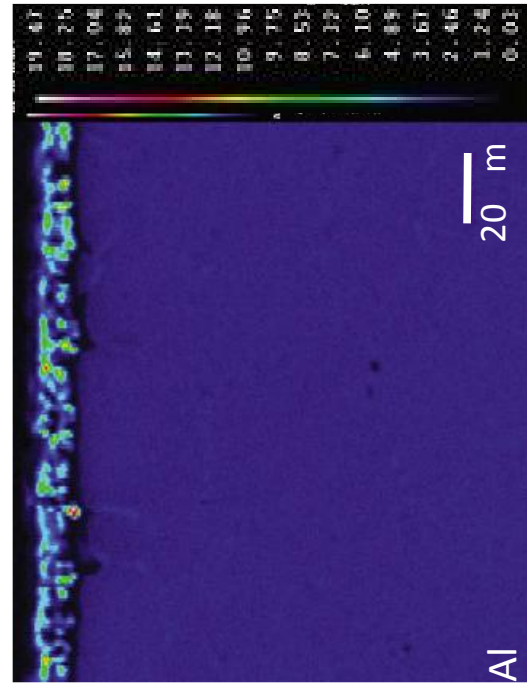
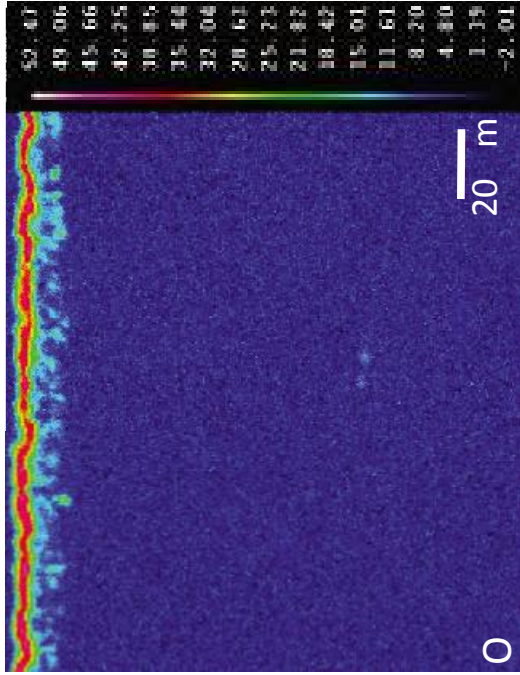
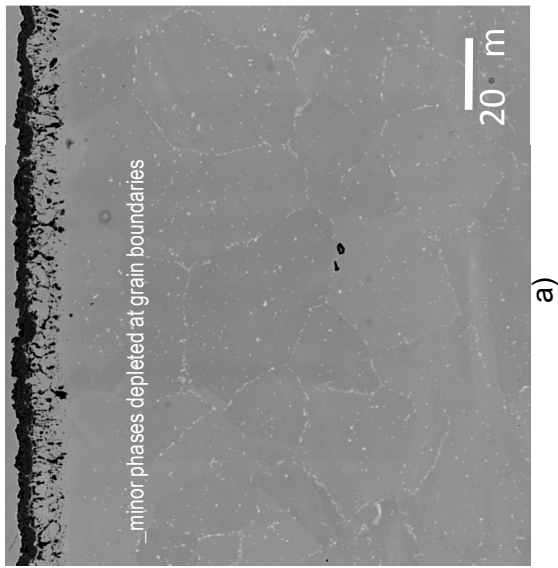


Fig. 6. Backscattered electron (BSE) image in a) shows area examined by electron microprobe in ME3 coupon exposed at 815 °C for 2,020 h. Composition dot maps indicate levels in weight % of O, Al, and Ti, which change near the surface.

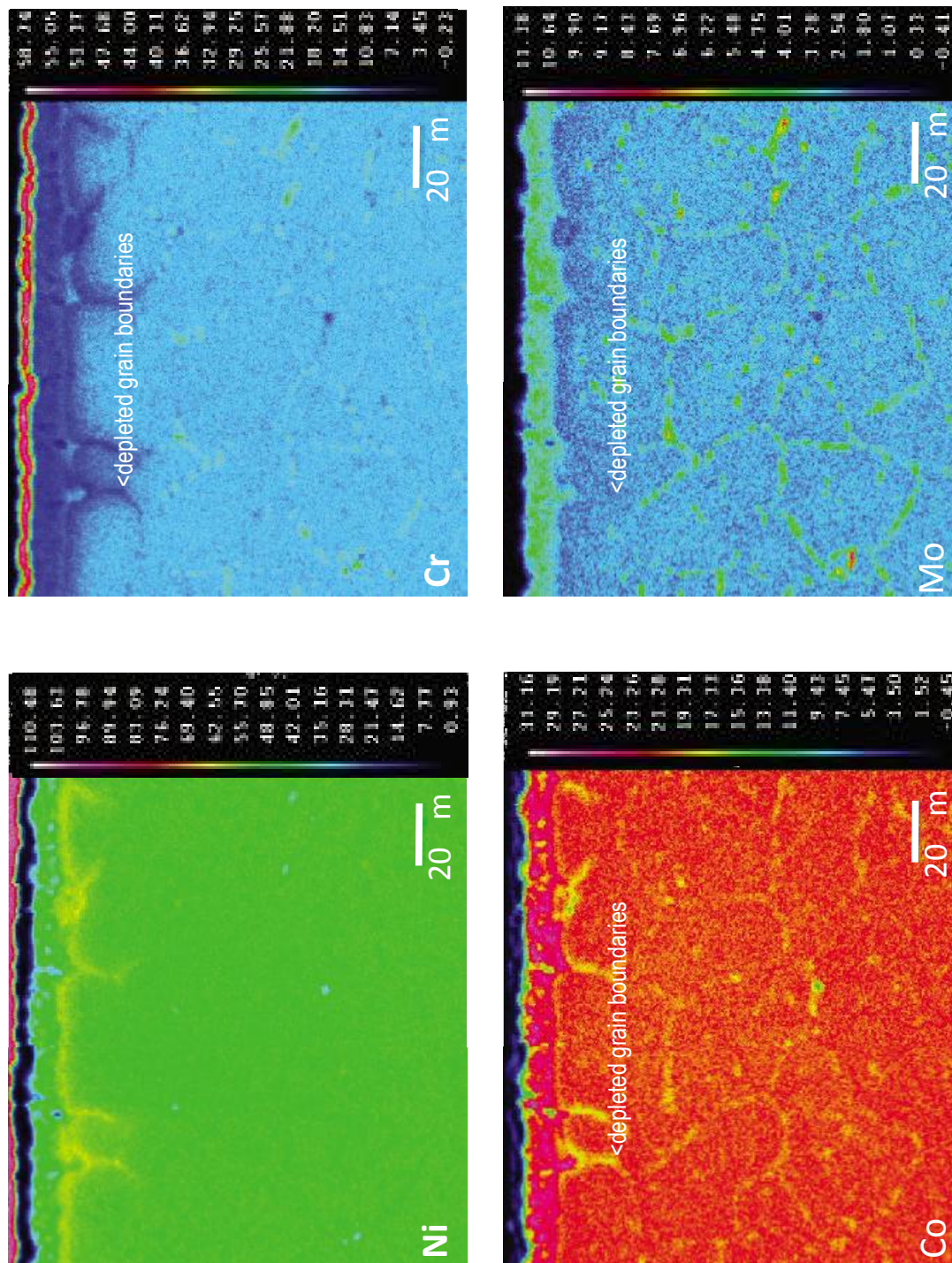


Fig. 6 (cont.) Composition dot maps indicating levels in weight % of Ni, Cr, Co, and Mo, which change near the surface.

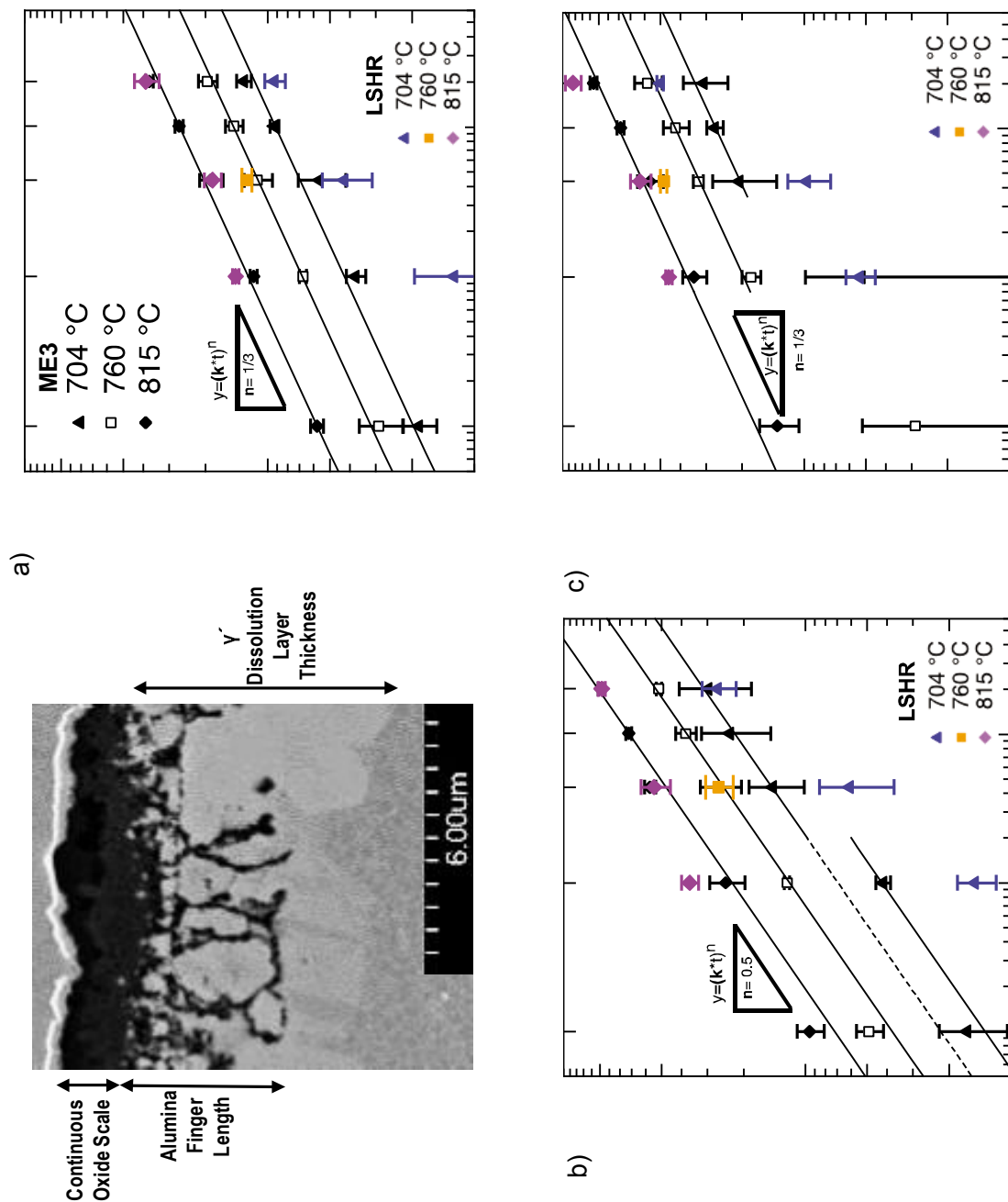


Fig. 7. Comparison of thicknesses for different surface zones of exposed coupons for ME3 and LSHR, a) continuous oxide scale thickness, b) alumina finger length, and c)  $\gamma'$ -dissolution layer thickness. Black symbols and lines remark the data and power-law fits for ME3, brackets indicate standard errors.

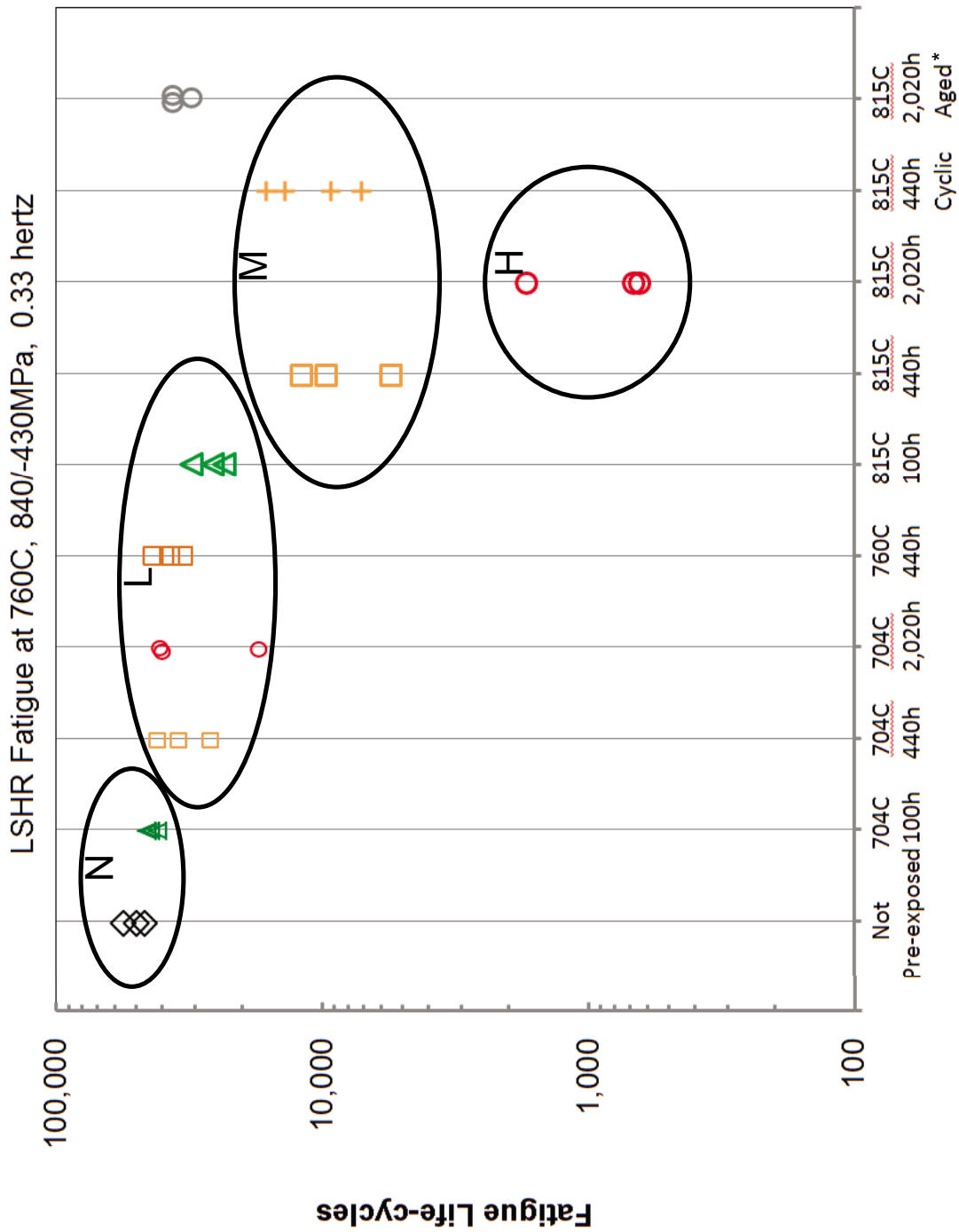


Fig. 8. Effect of prior exposures on fatigue lives of uniform-gage LSHR specimens, with failure groups N (no effects), L (low effects), M (medium effects), and H (high effects) indicated. \* Blanks aged 815 °C for 2,020 h before machining specimens. All other exposures were performed in air prior to testing on machined specimens.



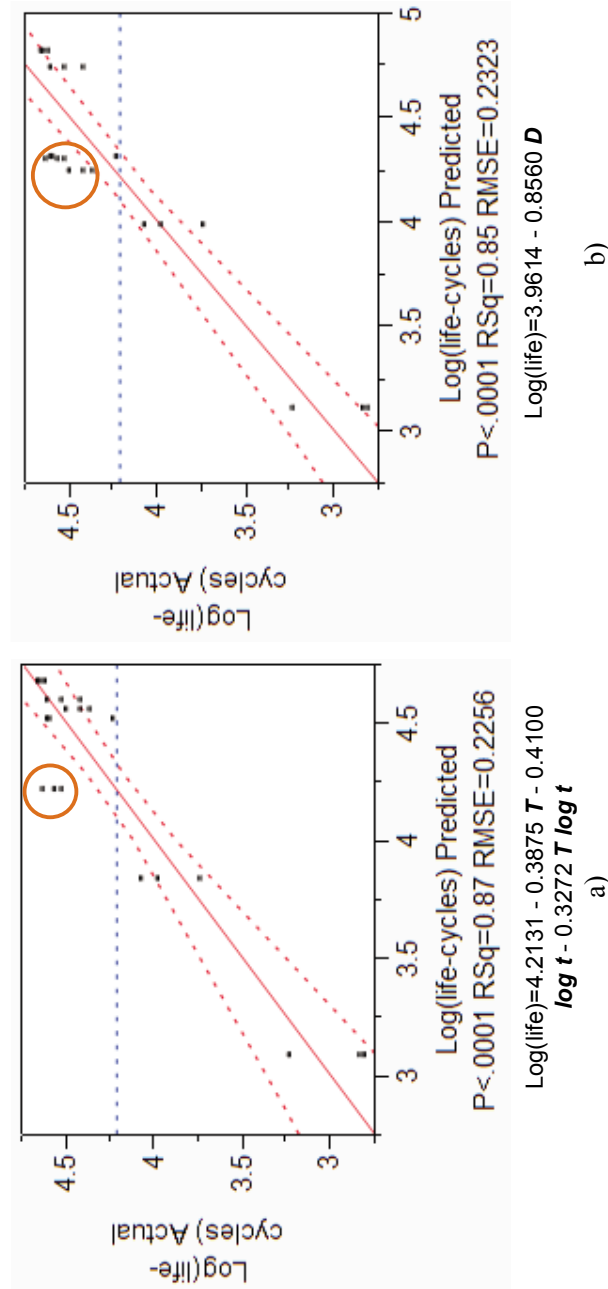


Fig. 9. Linear regressions of fatigue lives of uniform-gage LSHR specimens: a) Actual versus estimated log(life) using stepwise regression of exposure temperature, log(time), and their interaction; b) Actual versus estimated log(life) using regression of total damage depth = outer oxide scale thickness + inner finger depth + dissolution depth. 95% confidence intervals of estimated values indicated in red, RMSE - root mean square error. Points of poor agreement indicated in orange circles.

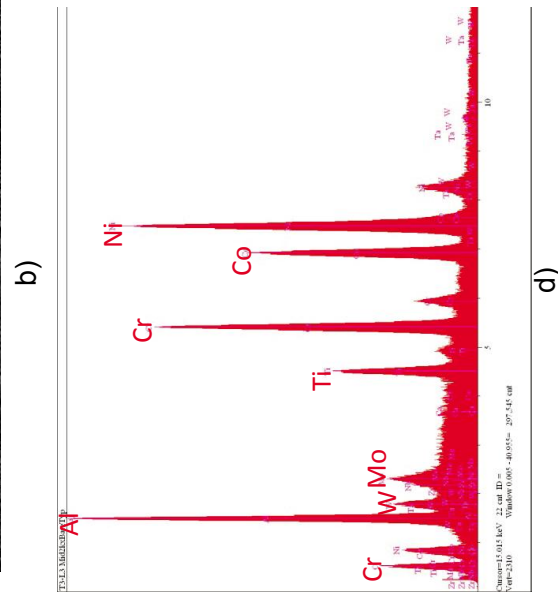
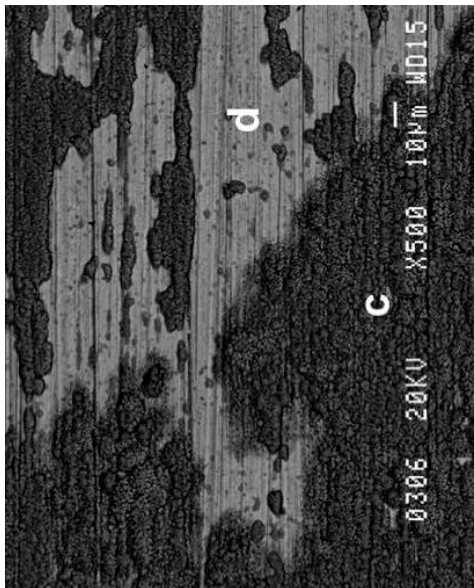
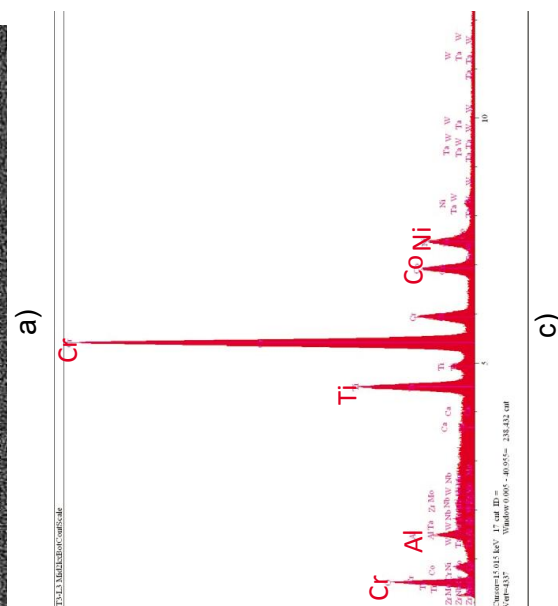
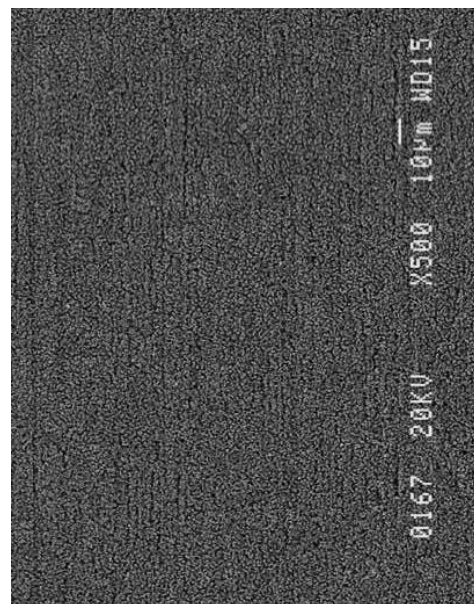
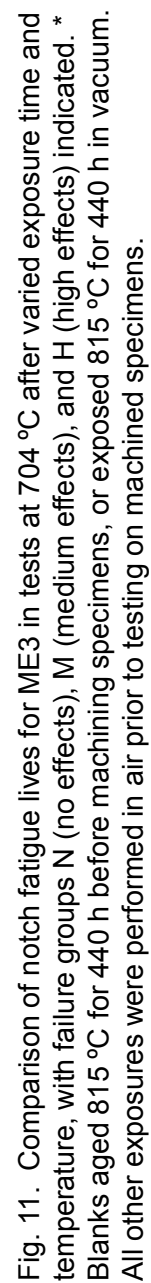


Fig. 10. Comparison of LSHR specimen surfaces before fatigue testing: a) 815 °C-440 h isothermal, and b) cyclic exposures, with a local discontinuity observed after cyclic exposure; c) chromium-rich oxide top layer was generally present for both exposures, including near discontinuity, and d) underlying aluminum-rich oxide layer was uncovered at discontinuity.



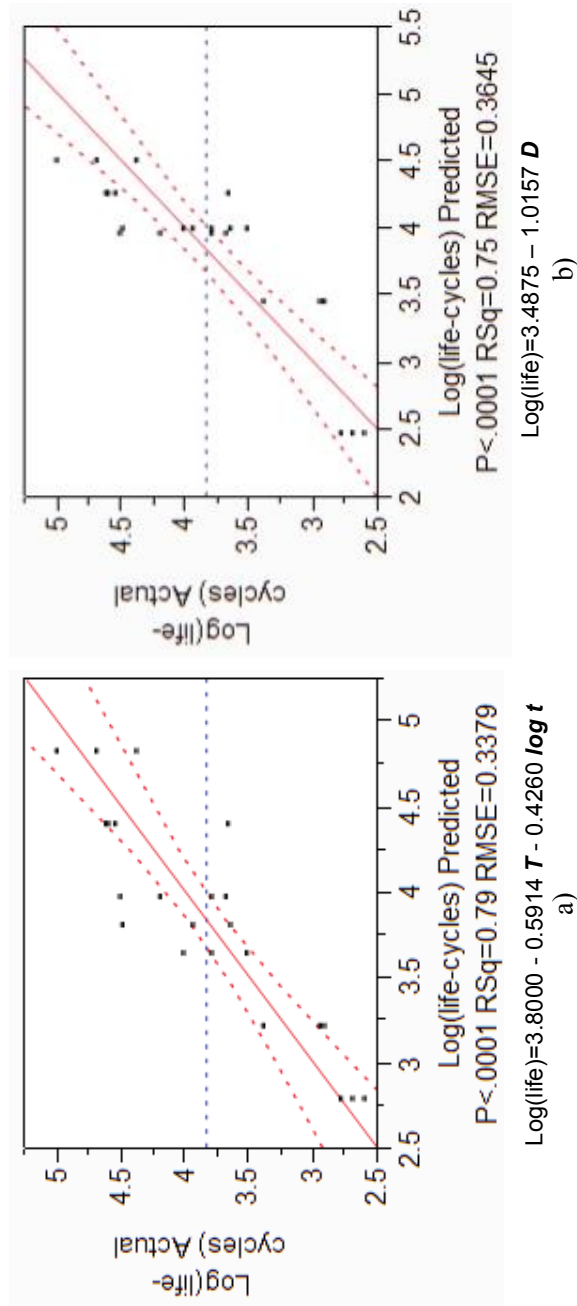


Fig. 12. Linear regressions of fatigue lives of ME3 notch fatigue specimens: a) Actual versus estimated  $\log(\text{life})$  using stepwise regression of exposure temperature,  $\log(\text{time})$ , and their interaction; b) Actual versus estimated  $\log(\text{life})$  using regression of total damage depth = outer oxide scale thickness + inner finger depth + dissolution depth. 95% confidence intervals of estimated values indicated in red, RMSE - root mean square error.



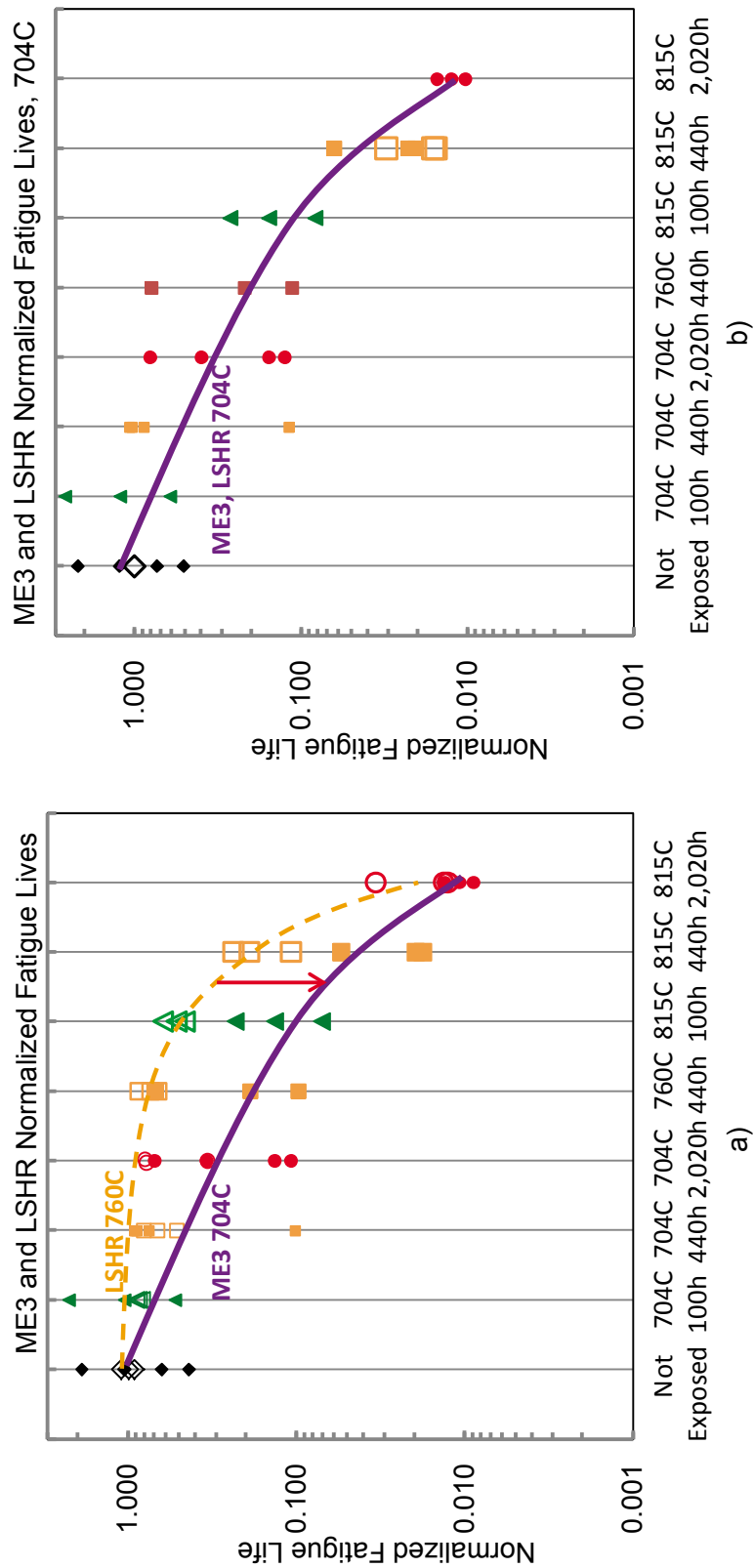


Fig. 13. Effects of prior exposures of machined specimens in air on fatigue lives, normalized by mean unexposed fatigue lives: a) ME3 notched specimens tested at 704 °C (filled symbols) and LSHR uniform gage specimens tested at 760 °C (open symbols), with arrow indicating difference in response at intermediate exposure conditions, b) ME3 and LSHR notched specimens tested at 704 °C, showing comparable response.

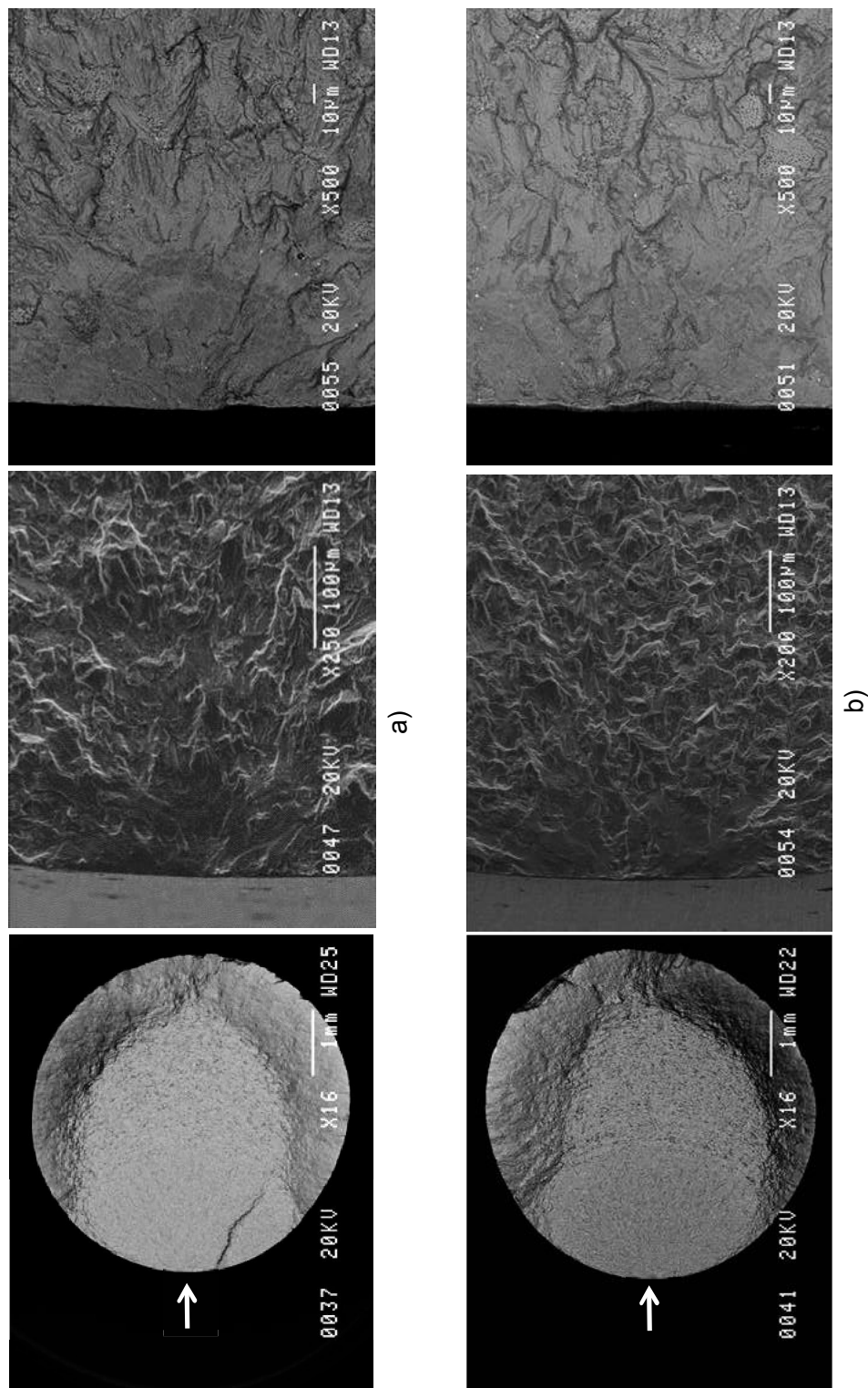


Fig. 14. Typical fracture surfaces for LSHR group N specimens: a) T3-L1, 704 °C-100 h, 41,624 cycles; b) T3-L17, no exposure, 55,123 cycles.

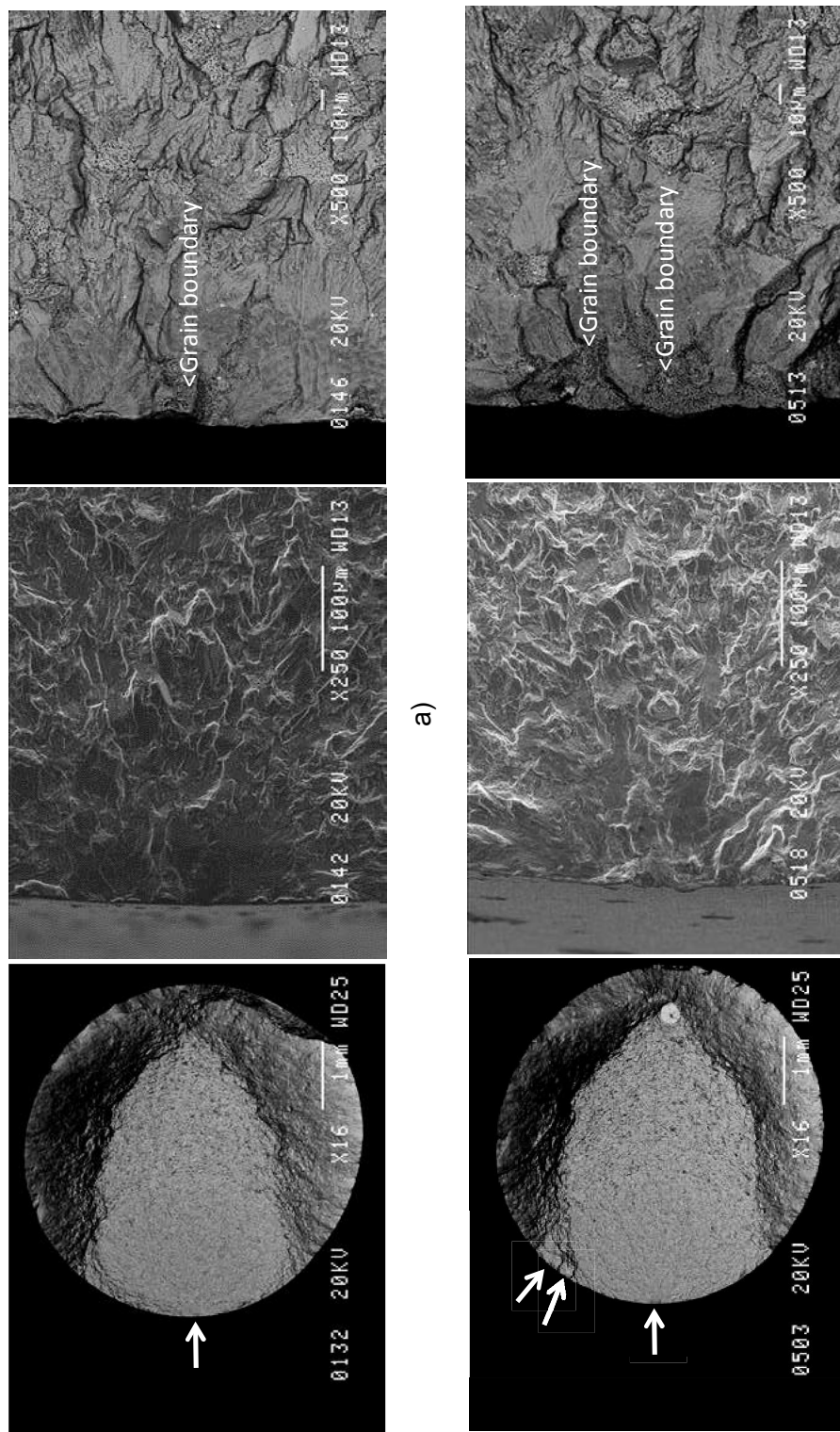


Fig. 15. Typical fracture surfaces for LSHR group L specimens: a) T3-L2, 704 °C-440 h, 25,734 cycles; b) T3-L11, 760 °C-440 h, 43,119 cycles.

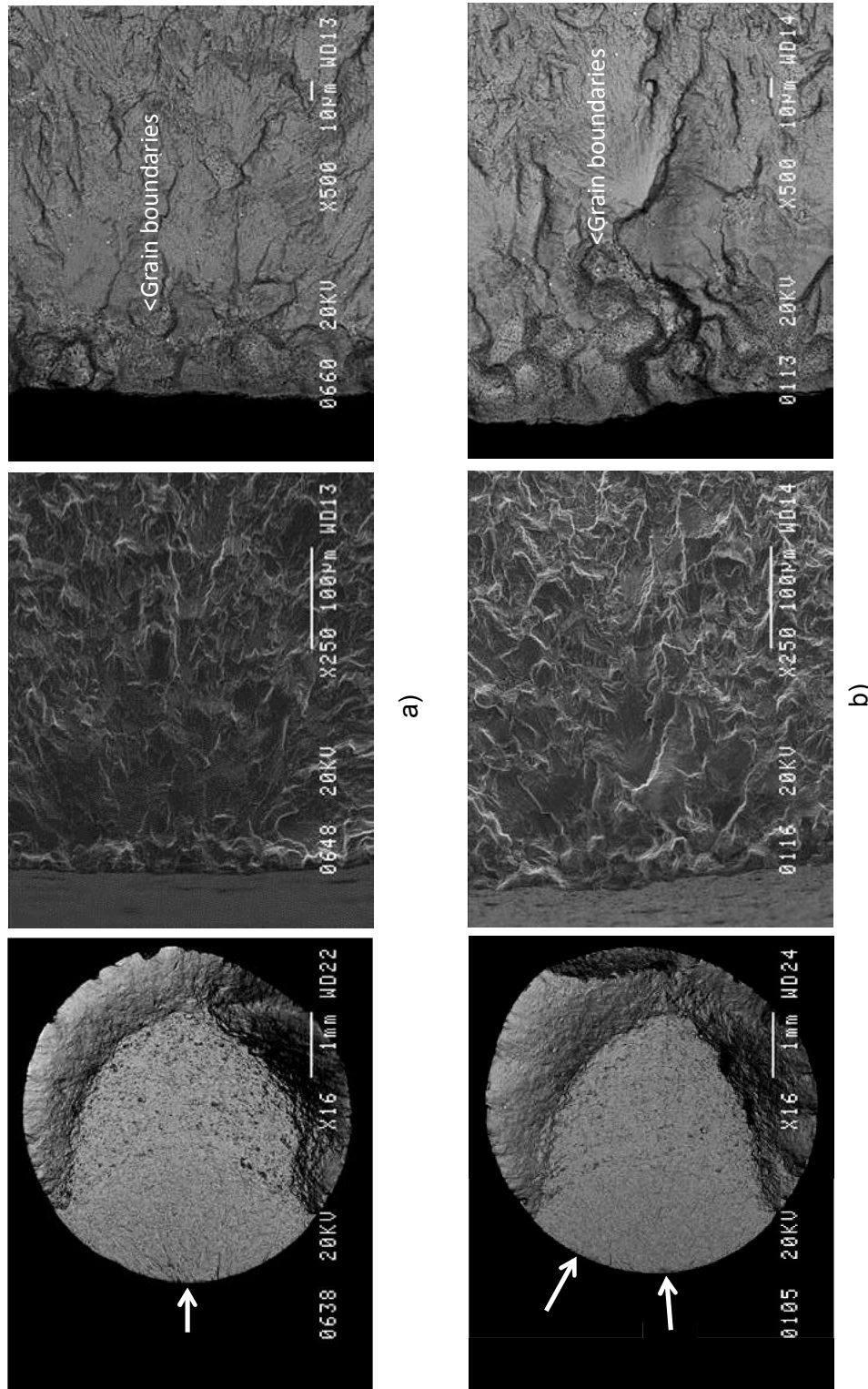


Fig. 16. Typical fracture surfaces for LSHR group M specimens: a) T3-L10, 815 °C-440 h constant exposure, 5,417 cycles; b) T3-L9, 815 °C-440 h cyclic exposure, 16,172 cycles.

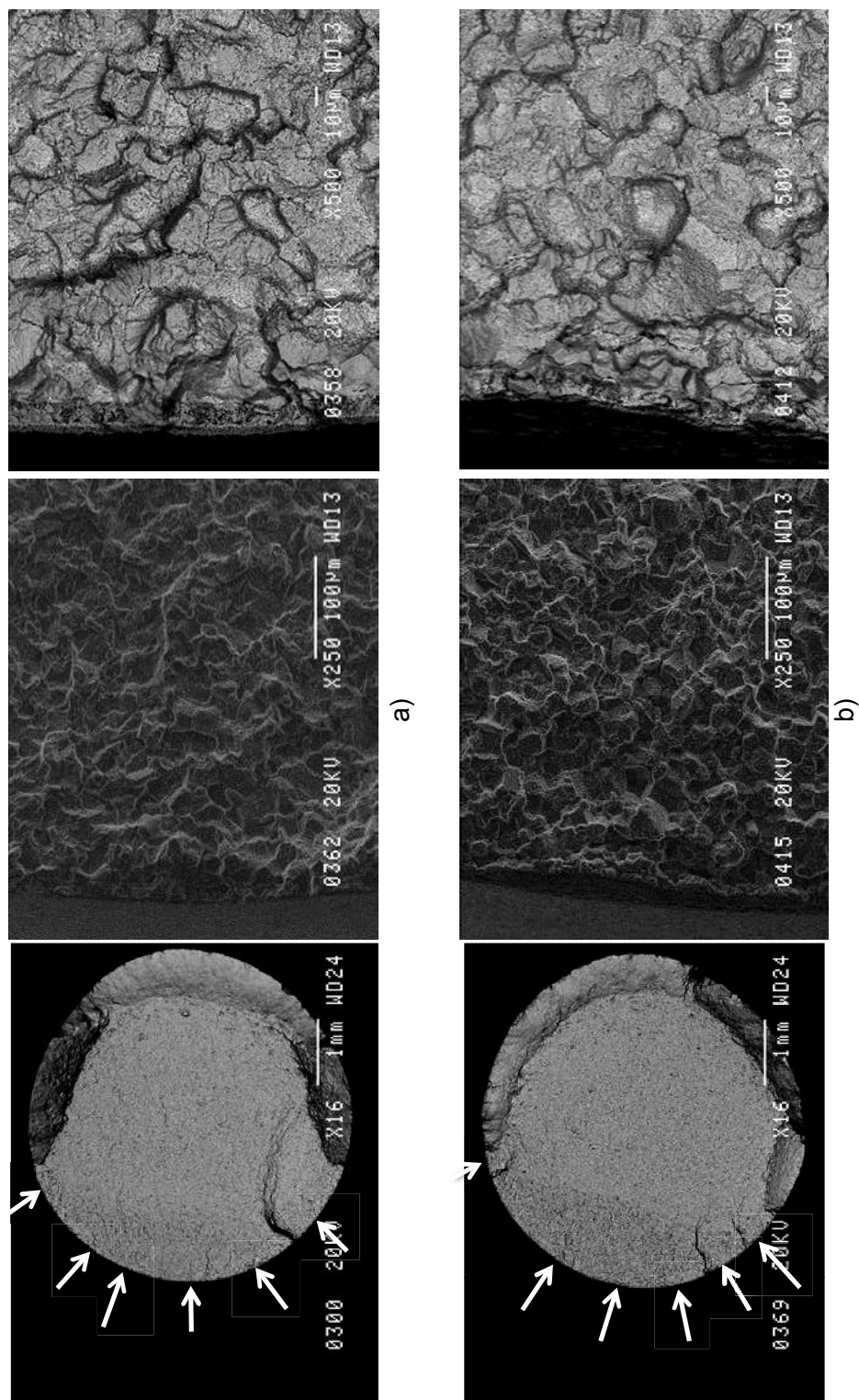


Fig. 17. Typical fracture surfaces showing intergranular crack initiation and growth for LSHR group H specimens:  
a) T3-L7, 815 °C-2,020 h, 669 cycles; b) Z6-L2, 815 °C-2,020 h, 1695 cycles.

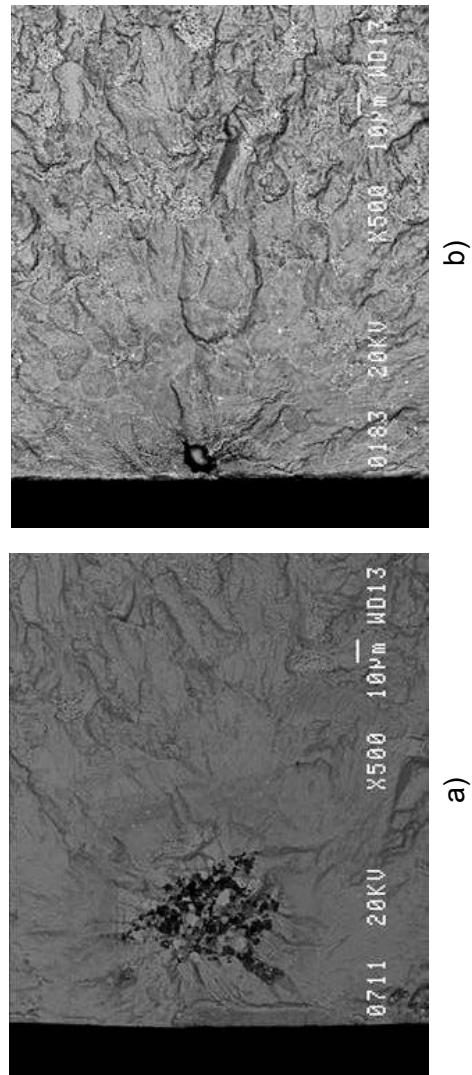


Fig. 18. Failure initiation sites for other LSHR specimens: a) T3-L12, no exposure, failed at 22,257 cycles from near-surface aluminum oxide inclusion; b) Z6-L17, Aged 815 °C-2,020 h, failed at 36,482 cycles from near-surface pore.



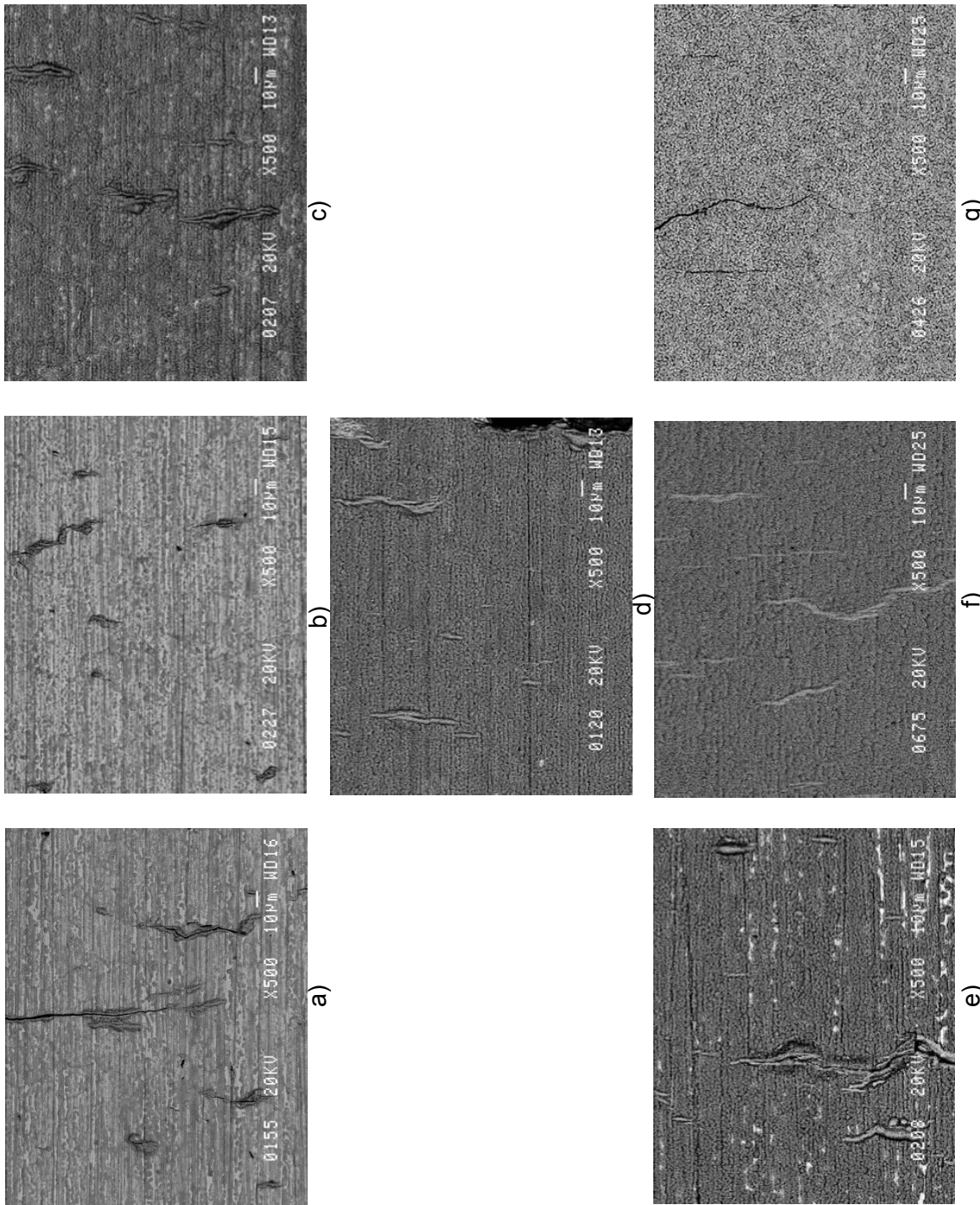


Fig. 19. Typical surface cracks after fatigue tests of LSHR at 760 °C: a) 704 °C-100 h, b) 704 °C-440 h, c) 704 °C-2,020 h, d) 760 °C-440 h, e) 815 °C-100 h, f) 815 °C-440 h, g) 815 °C-2,020 h.

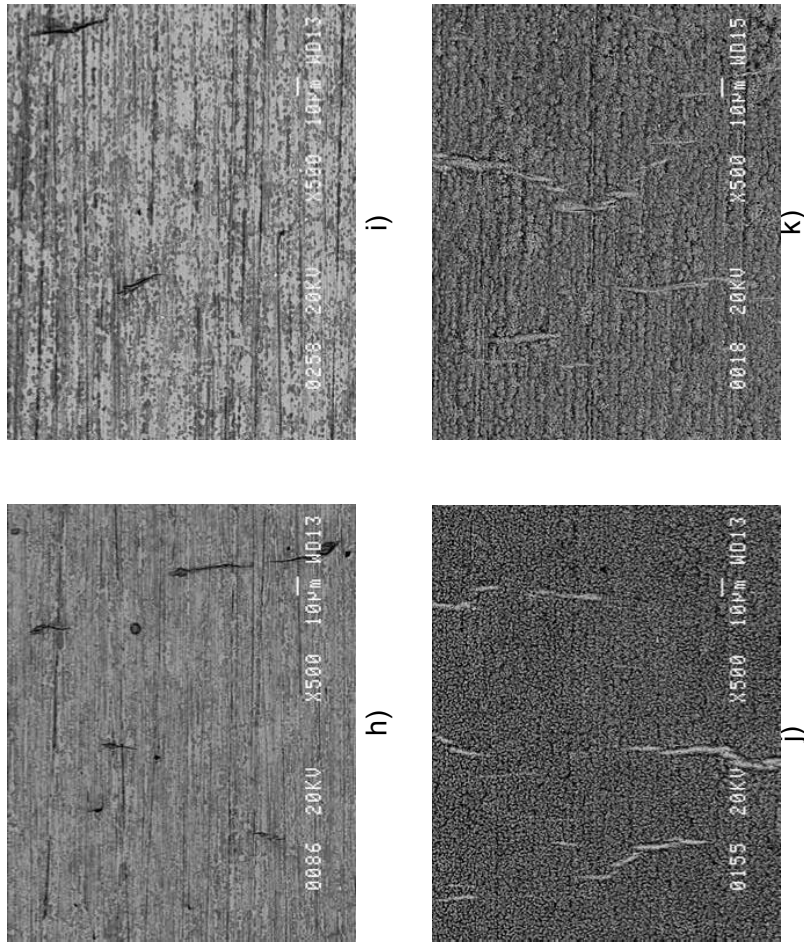


Fig. 19 (cont.). Typical surface cracks after fatigue tests of LSHR at 760 °C: h) No exposure, i) Aged 815 °C-2,020 h, j) Static exposure 815 °C-440 h, k) Cyclic exposure 815 °C-440 h.



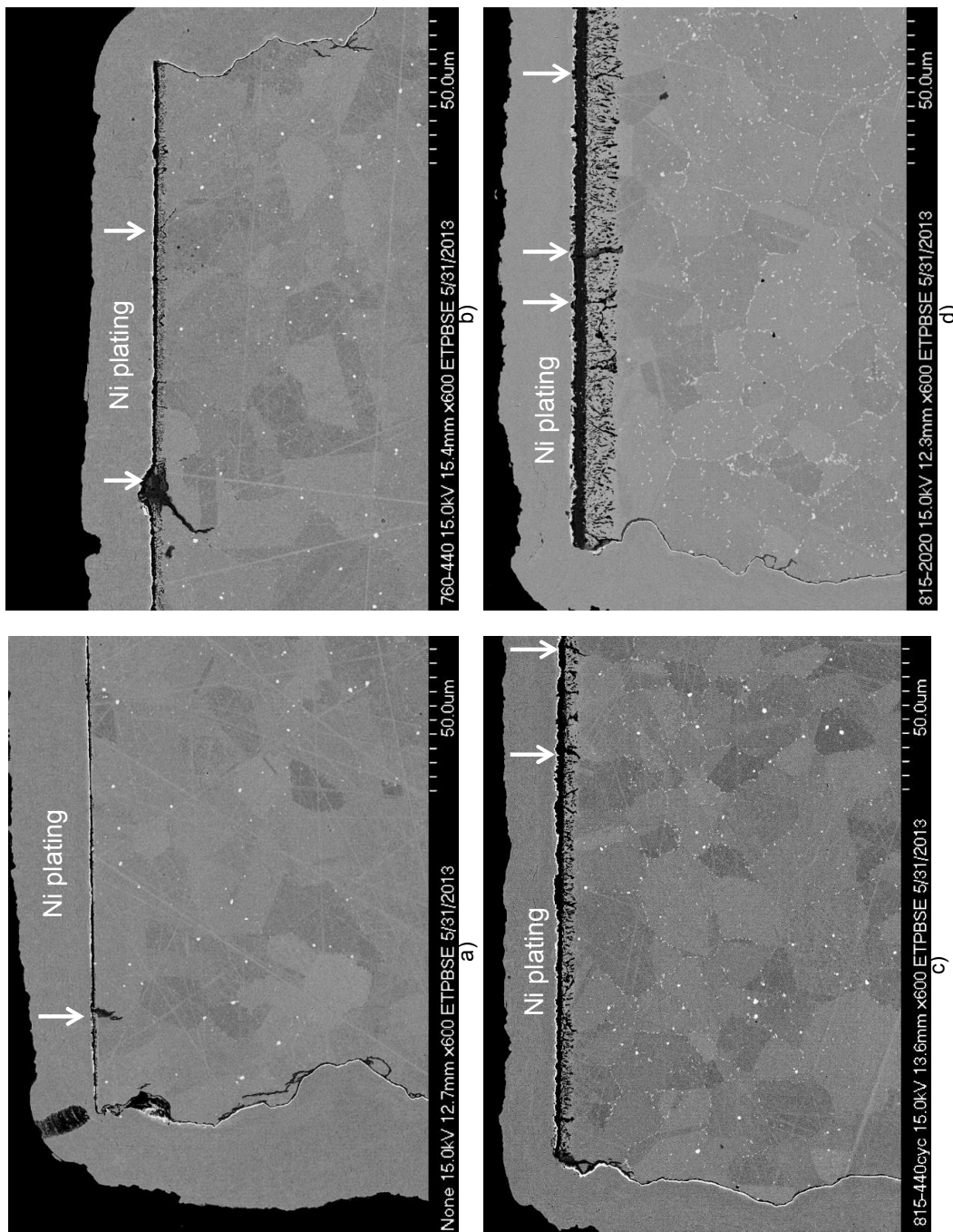


Fig. 20. Images showing surface cracks in longitudinal metallographic sections of LSHR specimens after fatigue tests at 760 °C: a) Group N, T3-L17, no exposure, 55,123 cycles; b) Group L, T3-L11, 760 °C-440 h, 43,119 cycles; c) Group M, T3-L9, 815 °C-440 h cyclic, 16,172 cycles; d) Group H, T3-L14, 815 °C-2,020 h, 635 cycles. Exposed surfaces were plated with Ni to preserve the oxide layers during metallographic preparation.

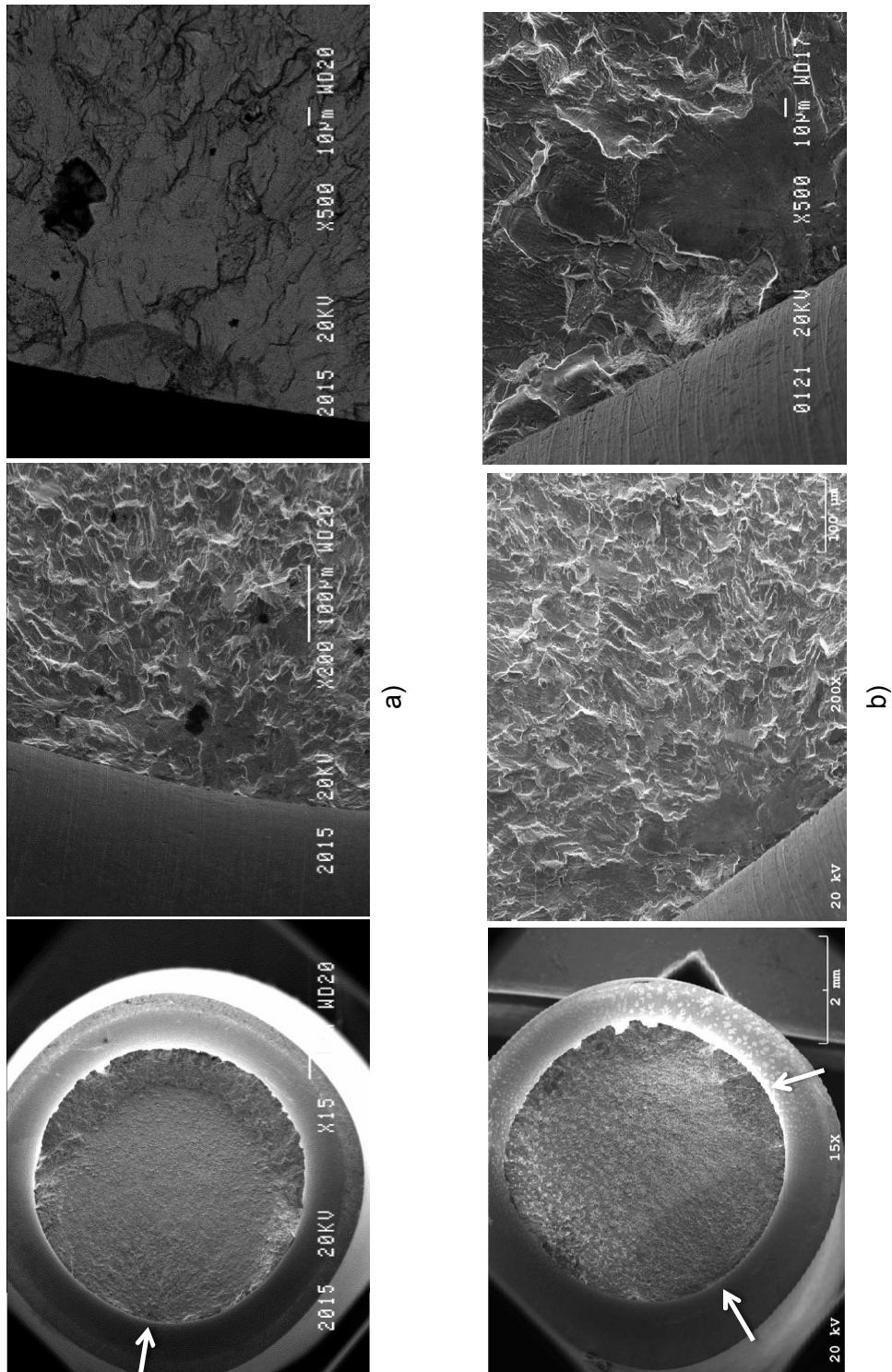


Fig. 21. Typical ME3 notched specimen fracture surfaces for group N: a) S101C-NER3, no exposure, 28,326 cycles; b) S101A-NER4, 704 °C-100 h, 100,256 cycles.

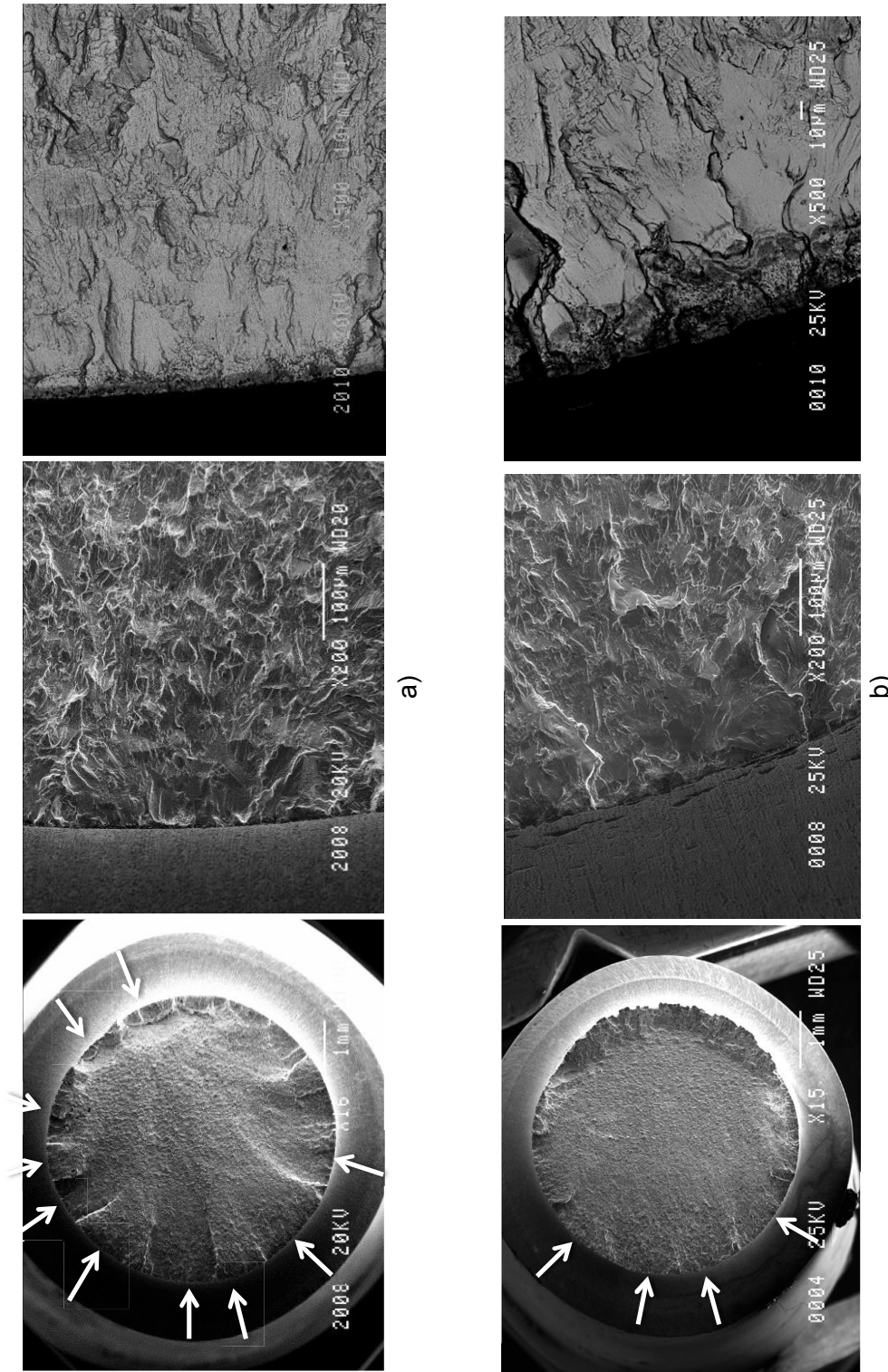


Fig. 22. Typical ME3 notched specimen fracture surfaces for group M, after static exposures: a) S101A-NER5, 815 °C-440 h, very many failure initiation points, 2,430 cycles; b) S101C-NER5, 760 °C-440 h, fewer failure initiation points, 30,472 cycles.

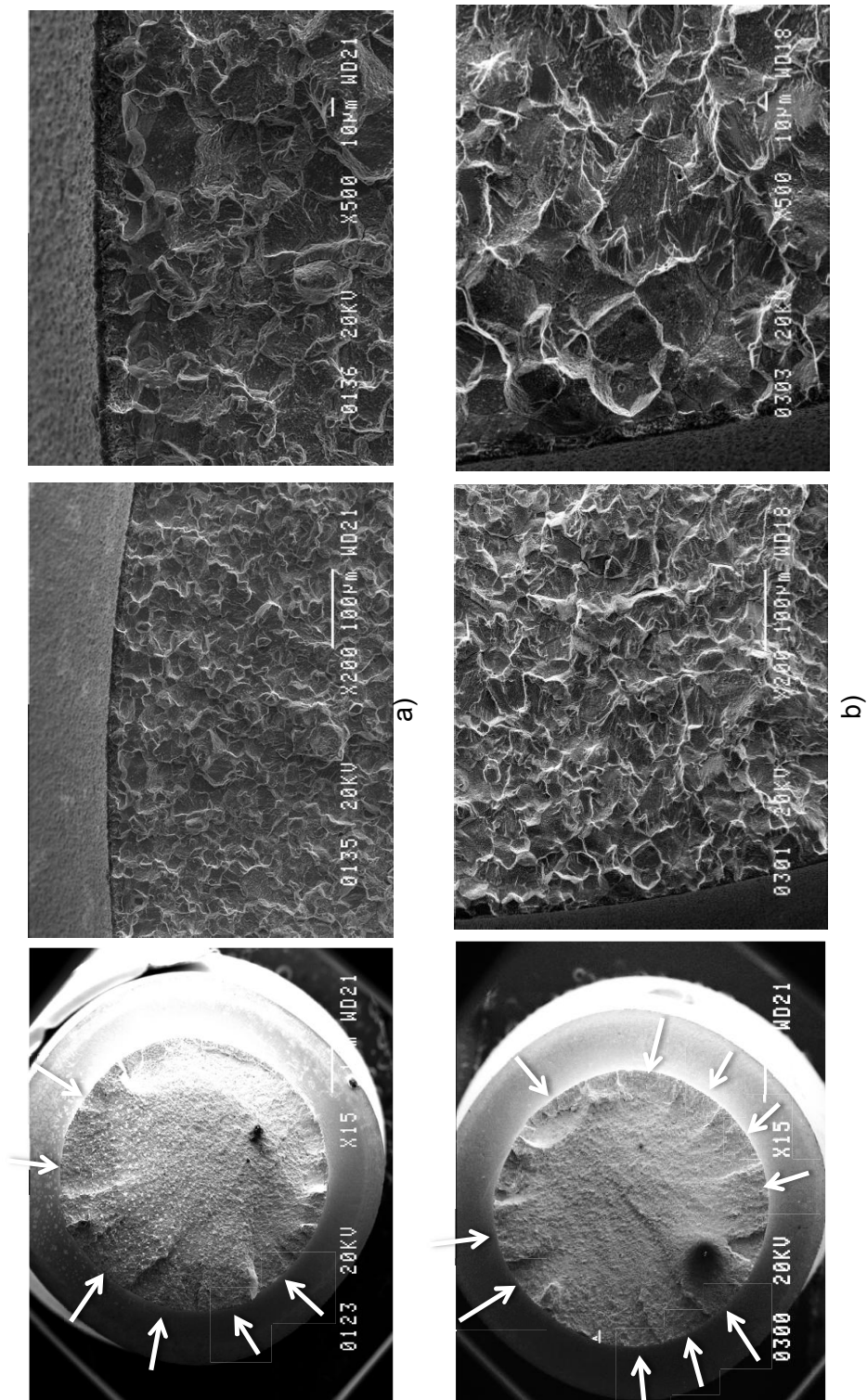


Fig. 23. Typical ME3 notched specimen fracture surfaces for group H, after static exposures: a) H101-NKR2, 815 °C-440 h, 874 cycles, b) H101-NKR5, 815 °C-440 h, 874 cycles.

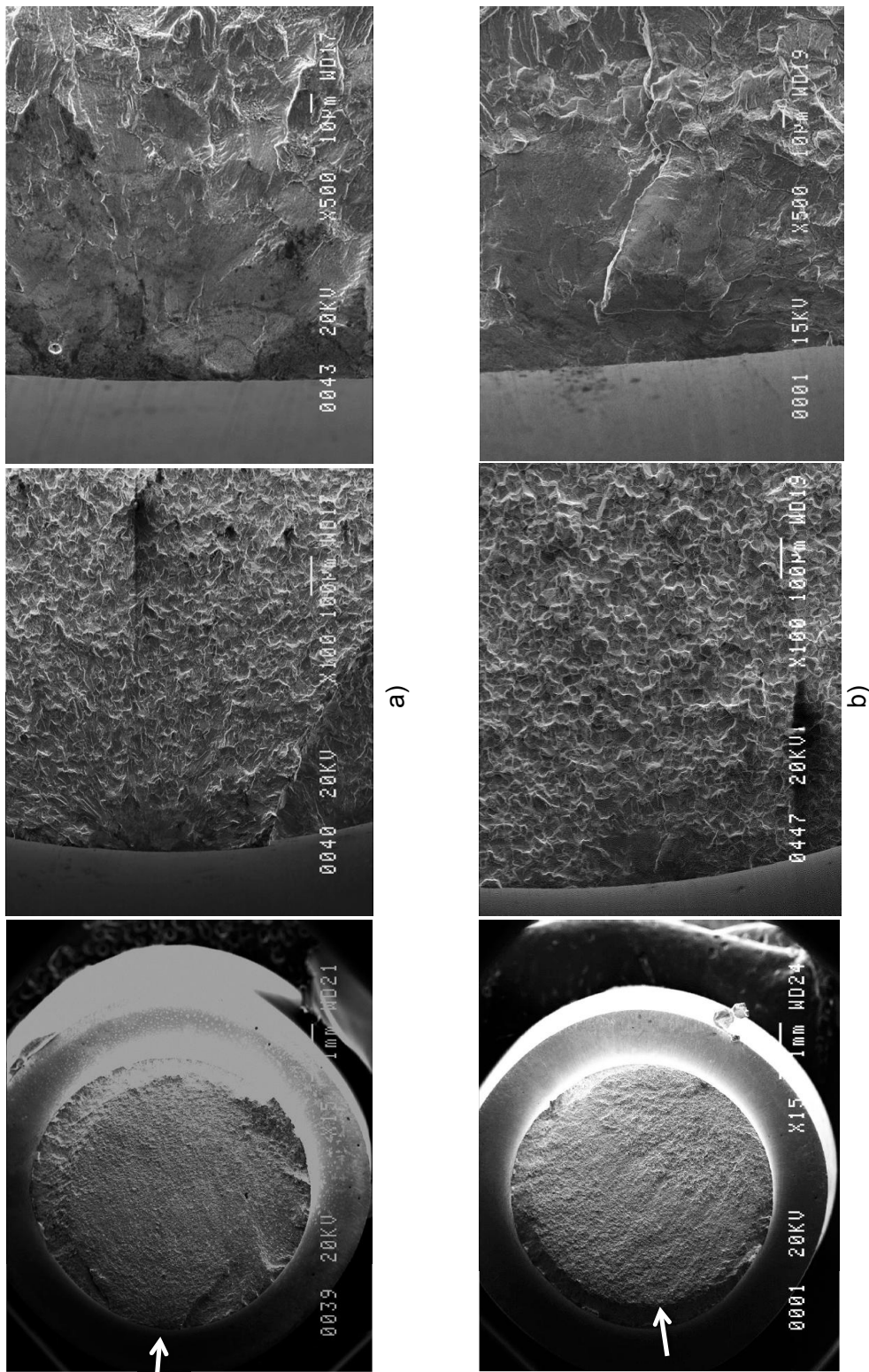


Fig. 24. Typical failure initiation sites of ME3 notched gage specimens, after altered conditions: a) exposed 815 °C-440 h in vacuum, S101A-NEW5, 53,309 cycles; b) Blank aged 815 °C-2,020 h before specimen machining, S101A-NEW1, 71,480 cycles.



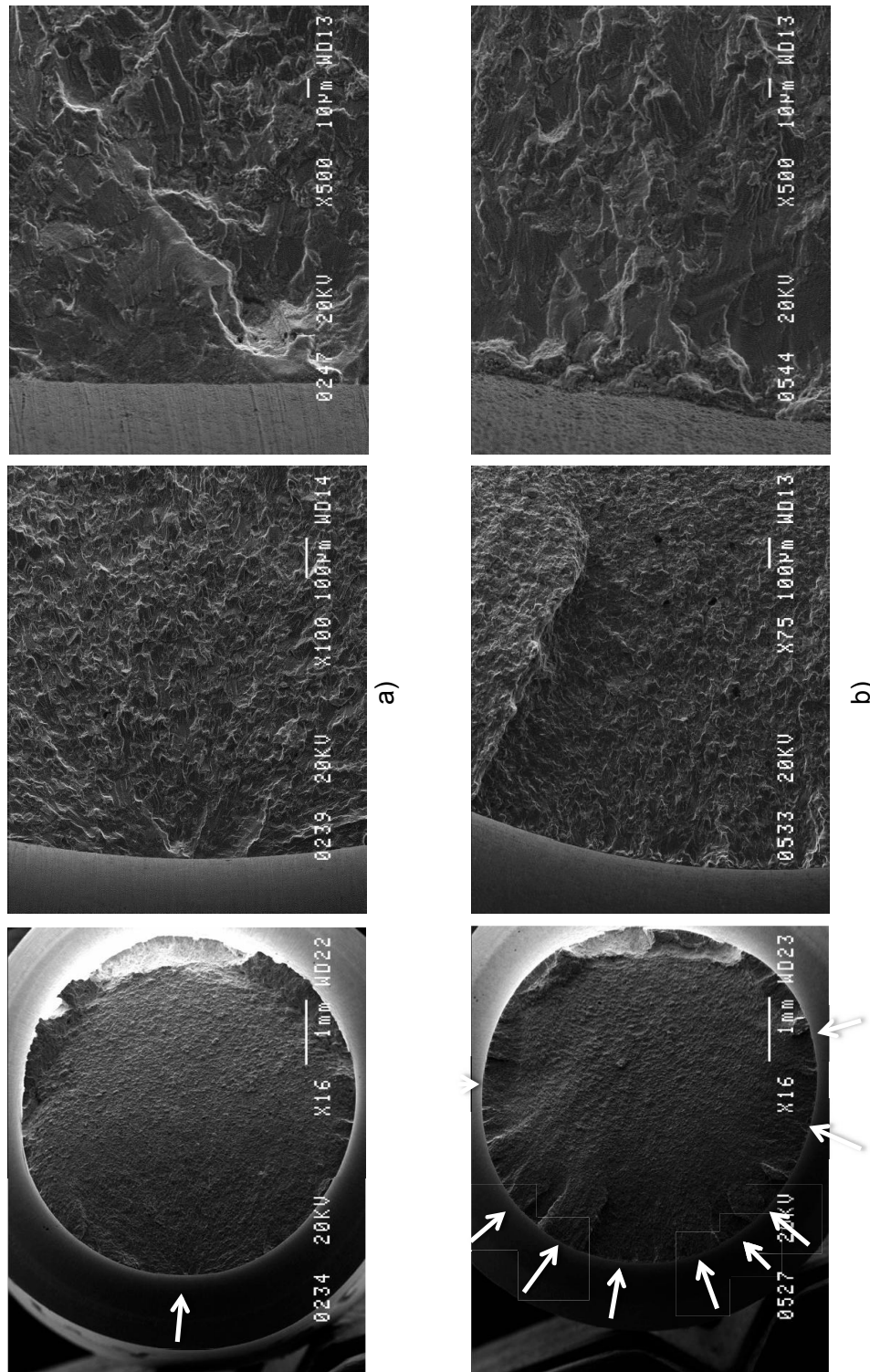


Fig. 25. Typical failure initiation sites of LSHR notched gage specimens, fatigue tested at 704 °C as per ME3 notched specimens: a) no exposure, T1W-SPL2, 154,692 cycles; b) Exposed 815 °C-440 h, T1N-SPL2, 2,481 cycles.

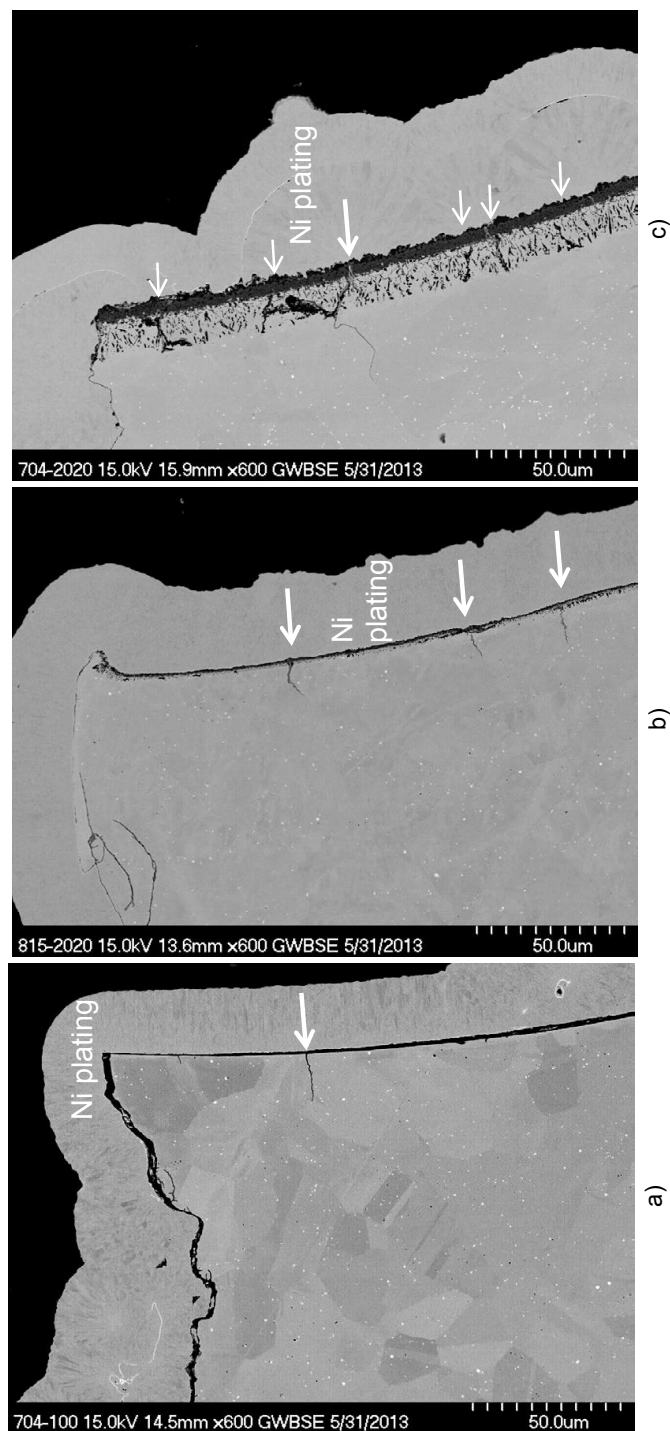


Fig. 26. Optical images for longitudinal metallographic sections of surface cracks after fatigue tests of ME3 at 704 °C: a) Group N, S101A-NER4, 704 °C-100 h, very few cracks, 100,256 cycles; b) Group M, S101B-NER9, 704 °C-2,020 h, showing more numerous cracks, 4,810 cycles; c) Group H, H101-NLR1, 815 °C-2,020 h, showing many cracks in recrystallized grain zone, 482 cycles. Exposed surfaces were plated with Ni to preserve the oxide layers during metallographic preparation.

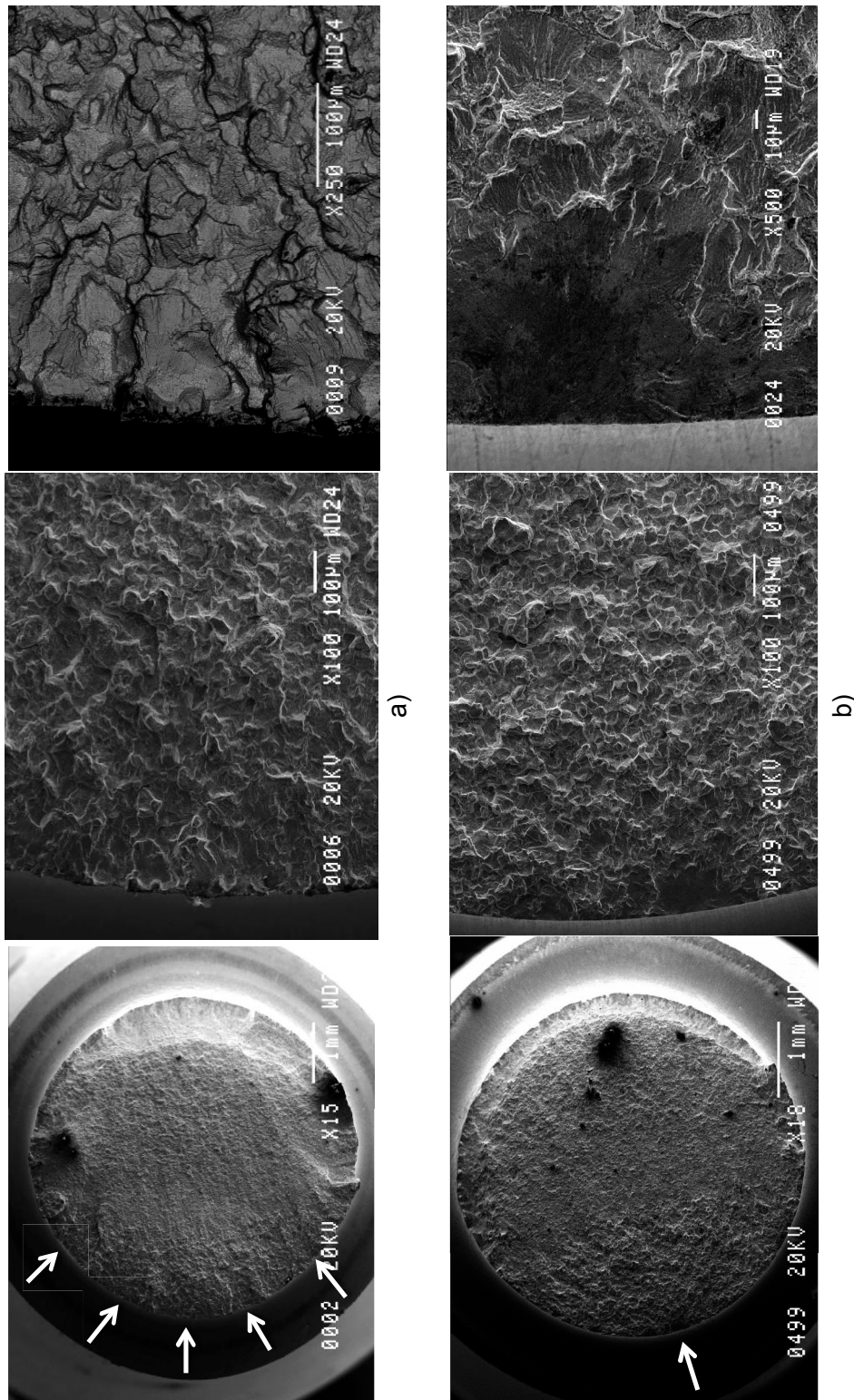


Fig. 27. Typical failure initiation sites of ME3 notched gage specimens, exposed at 815 °C-2,020 h in air, then polished to remove surface layers before fatigue testing: a) 20  $\mu\text{m}$  depth removed, S101B-NER8, 1,046 cycles; b) 50  $\mu\text{m}$  depth removed, S101A-NER8, 32,980 cycles.



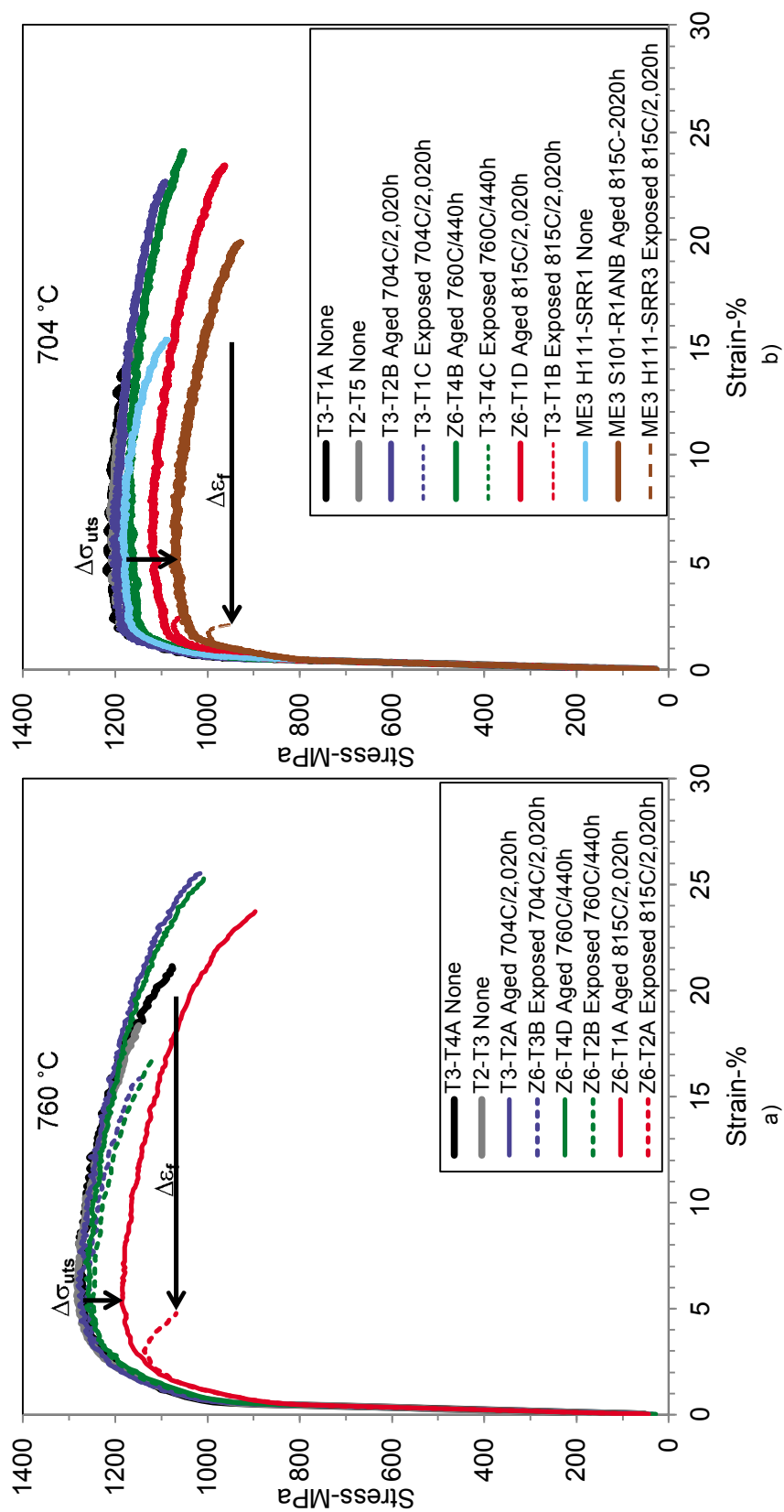


Fig. 28. Effects of prior static exposures in air or aging on tensile response in air: a) LSHR at 760 °C and 0.104 mm/s, b) LSHR and ME3 at 704 °C and 0.00173 mm/s. Conditions producing large reductions in strength ( $\Delta\sigma_{uts}$ ) and elongation ( $\Delta\epsilon_f$ ) indicated by arrows.

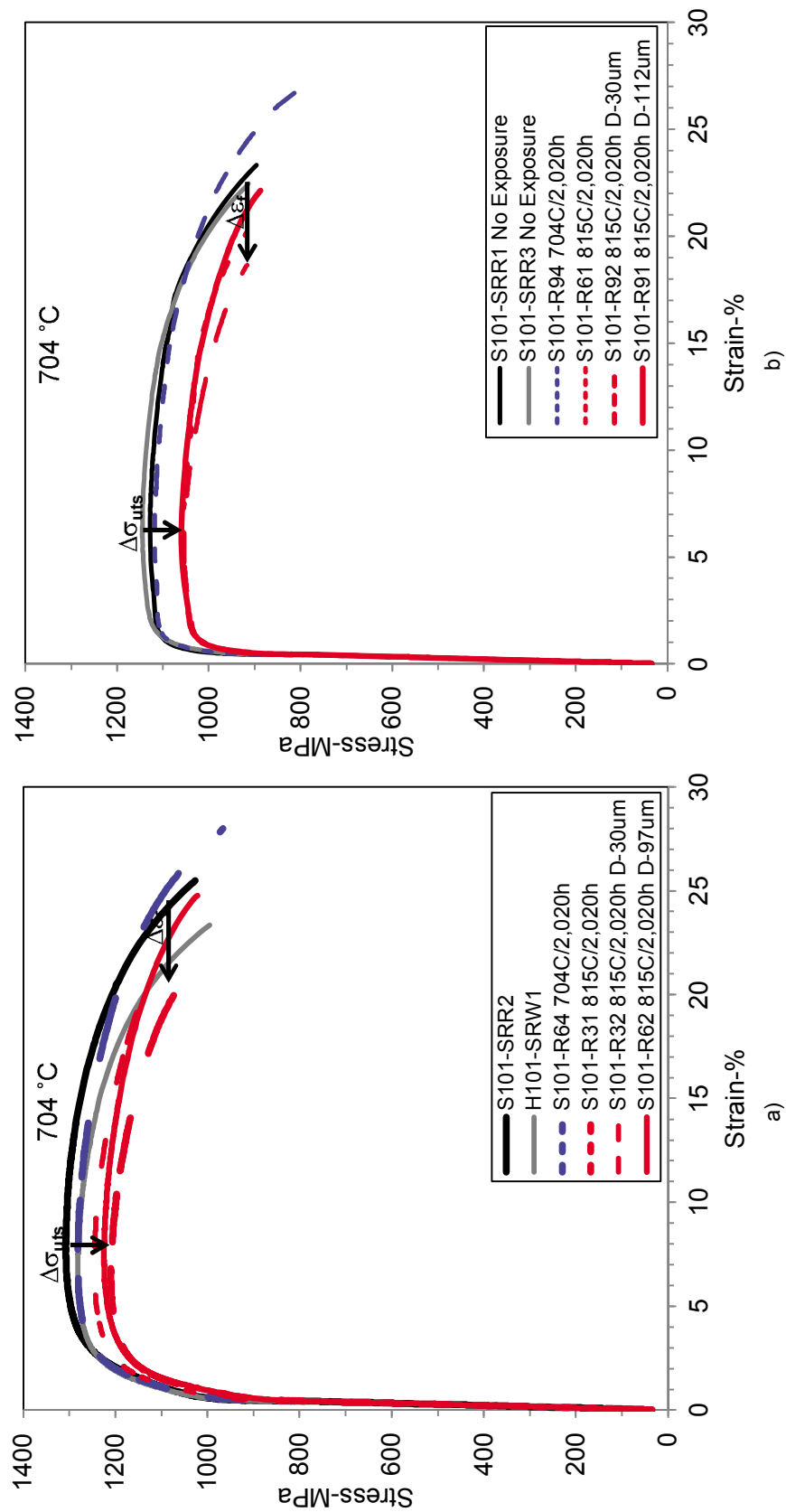


Fig. 29. Effect of prior static exposures in air on tensile response of ME3, tested in vacuum at 704 °C: a) 0.0173 mm/s, b) 0.00173 mm/s. Maximum reductions in strength ( $\Delta\sigma_{uts}$ ) and elongation ( $\Delta\epsilon_f$ ) indicated by arrows.

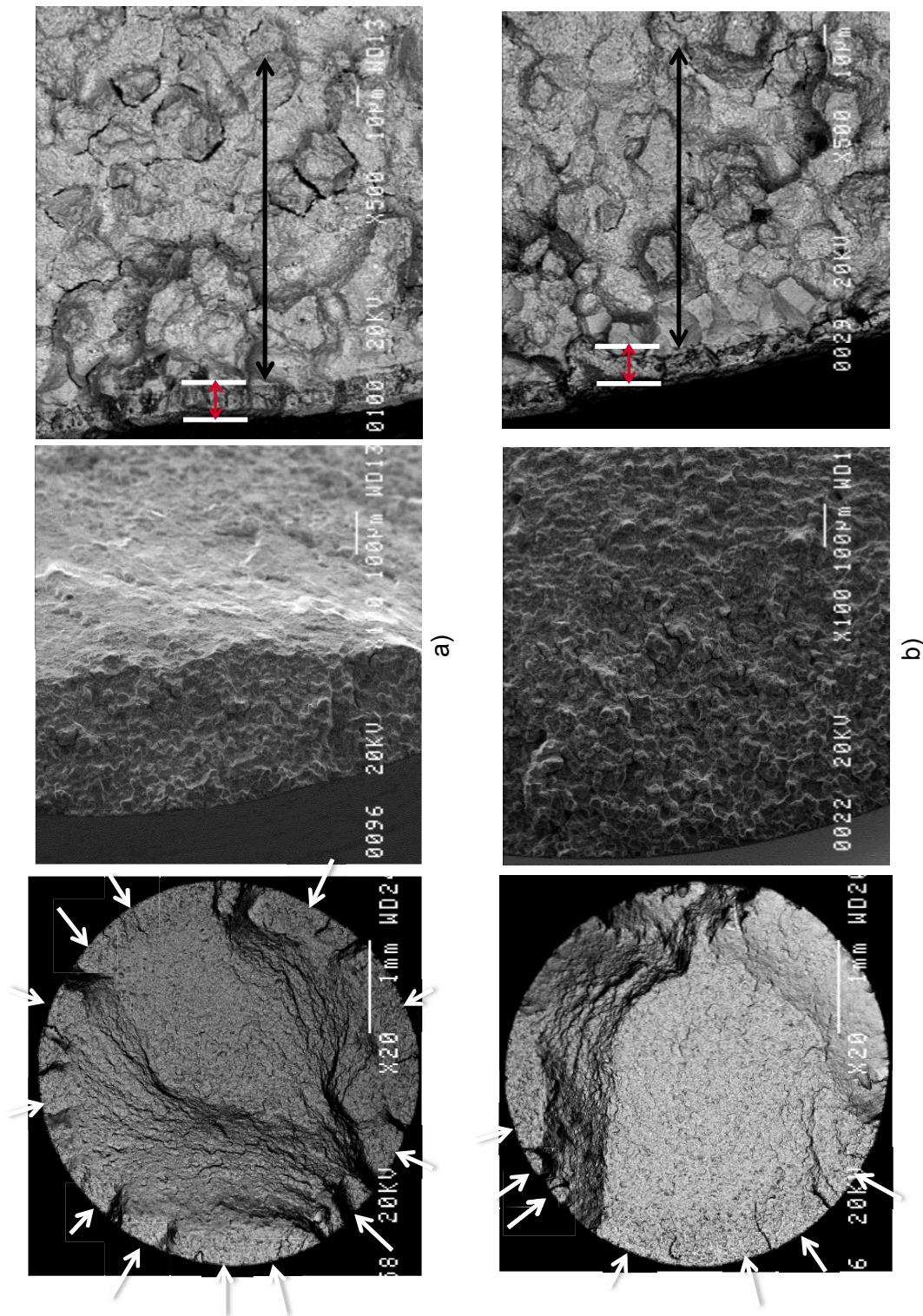


Fig. 30. Effect of prior static exposures in air on tensile failure modes: a) LSHR, Z6-T2A, exposed 815 °C-2,020 h, tested in air at 760 °C; b) LSHR, T3-T1B, exposed 815 °C-2,020 h, tested in air at 704 °C.



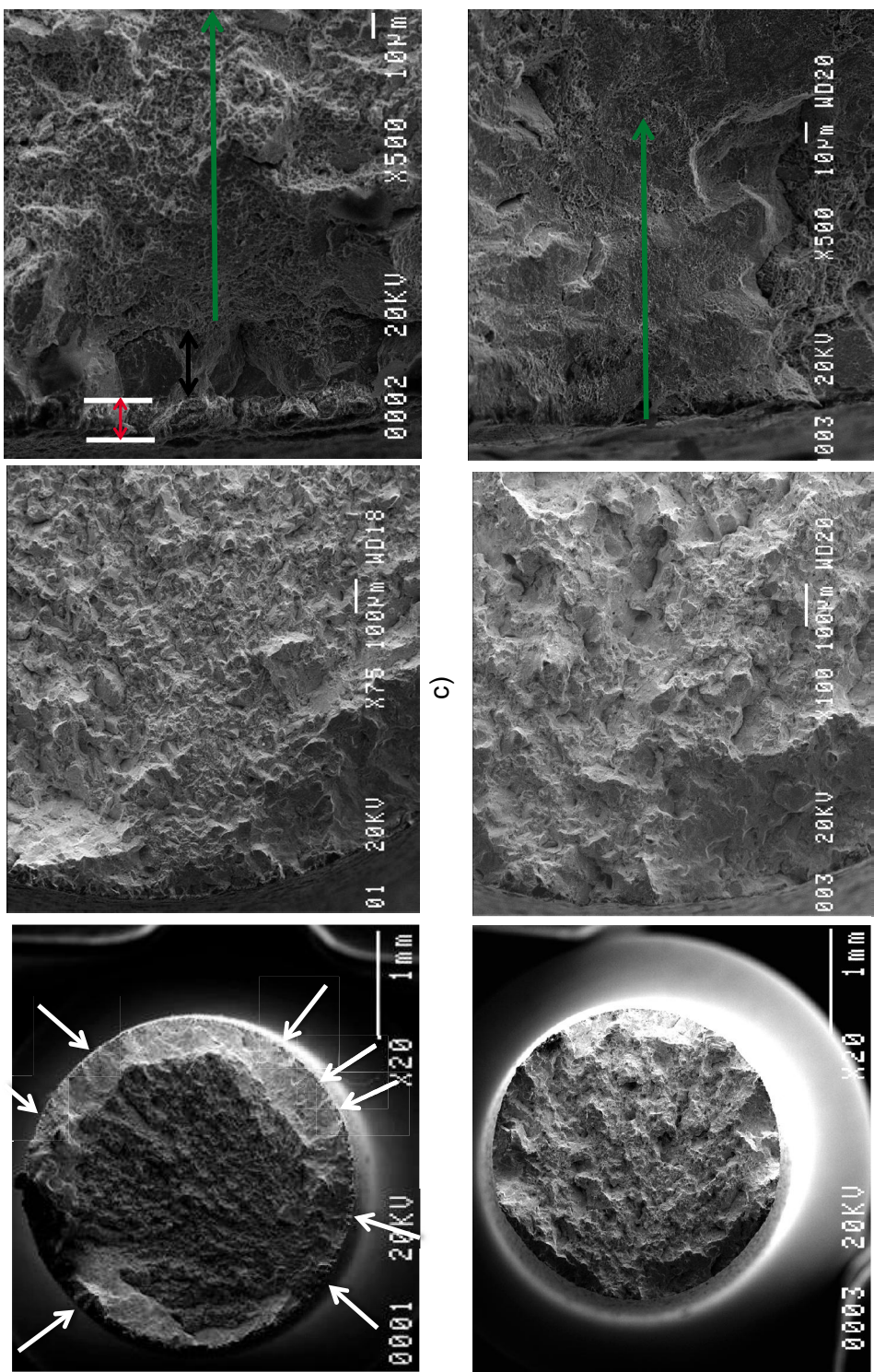


Fig. 30 (cont.) Effect of prior static exposures in air on tensile failure modes: c) ME3, S101-R31, exposed 815 °C -2,020 h, tested in vacuum at 704 °C, showing surface cracking of the outer oxide layers (red arrow), intergranular cracking of the minor phase depleted zone (white) as for LSHR, but internal transgranular failure (green); d) ME3, S101-R62, exposed 815 °C -2,020 h, 50 μm removed, tested in vacuum at 704 °C showing transgranular failure and highest reduction in area.



